Front. Phys., 2012, 7(3): 328–352
DOI 10.1007/s11467-011-0200-5

REVIEW ARTICLE

Electronic and optical properties of semiconductor and graphene quantum dots

Wei-dong Sheng[1,2,*], **Marek Korkusinski**[1], **Alev Devrim Güçlü**[1], **Michal Zielinski**[1,3], **Pawel Potasz**[1,4], **Eugene S. Kadantsev**[1], **Oleksandr Voznyy**[1], **Pawel Hawrylak**[1,†]

[1] *Institute for Microstructural Sciences, National Research Council of Canada, Ottawa, Canada*
[2] *Department of Physics, Fudan University, Shanghai 200433, China*
[3] *Institute of Physics, Nicolaus Copernicus University, Torun, Poland*
[4] *Institute of Physics, Wroclaw University of Technology, Wroclaw, Poland*
*E-mail: *shengw@fudan.edu.cn, †Pawel.Hawrylak@nrc-cnrc.gc.ca*
Received April 21, 2011; accepted July 27, 2011

Our recent work on the electronic and optical properties of semiconductor and graphene quantum dots is reviewed. For strained self-assembled InAs quantum dots on GaAs or InP substrate atomic positions and strain distribution are described using valence-force field approach and continuous elasticity theory. The strain is coupled with the effective mass, $\boldsymbol{k}\cdot\boldsymbol{p}$, effective bond-orbital and atomistic tight-binding models for the description of the conduction and valence band states. The single-particle states are used as input to the calculation of optical properties, with electron-electron interactions included via configuration interaction (CI) method. This methodology is used to describe multiexciton complexes in quantum dot lasers, and in particular the hidden symmetry as the underlying principle of multiexciton energy levels, manipulating emission from biexcitons for entangled photon pairs, and optical control and detection of electron spins using gates. The self-assembled quantum dots are compared with graphene quantum dots, one carbon atom-thick nanostructures. It is shown that the control of size, shape and character of the edge of graphene dots allows to manipulate simultaneously the electronic, optical, and magnetic properties in a single material system.

Keywords quantum dots, electronic structure, multiexciton, graphene, magnetism

PACS numbers 78.67.Hc, 73.21.La, 73.63.Kv, 73.22.Pr

Contents

1 Introduction

In this article we highlight some of our recent works towards the understanding of electronic and optical properties of semiconductor [1–5] and graphene quantum dots [6]. The recent research on semiconductor quantum dots follows naturally the evolution of semiconductor technology from transistors and lasers based on bulk silicon and bulk gallium arsenide to field effect transistors and quantum-well lasers. In these systems, the control of material composition in one dimension, e.g., molecular beam epitaxy has led to integrated circuits and revolutionary changes in information technology. Semiconductor quantum dots are a natural step forward in allowing for the control of material composition in three dimensions and at the nanoscale. Hence quantum dots are an example of nanoscience and nanotechnology in semiconductors. There are four major classes of quantum dots: (i) lateral gated quantum dots, (ii) self-assembled quantum dots, (iii) colloidal nanocrystals, and the most recent addition, (iv) graphene quantum dots.

The lateral gated quantum dots are created at a semiconductor GaAlAs/GaAs heterojunction containing a two-dimensional electron gas as in the field-effect transistor (FET). On top of the GaAs surface a pattern of metallic gates with nanometer dimensions is deposited. When negative voltage is applied to the gates, electrons residing underneath these gates at the GaAlAs/GaAs heterojunction feel repulsive potential and are pushed out from under the gates [1, 3]. By designing the gates in such a way that the repulsive potential under the gates seen by electrons resembles a volcano, a controlled number of electrons, down to one, can be trapped in the volcano's crater. The counting of electrons in the lateral quantum dot and subsequent isolation of a single electron have been demonstrated at the Institute for Microstructural Sciences [7–9]. It is now possible to construct double [10–13] and triple quantum dot molecules [14–17] where individual electrons are isolated, quantum mechanically coupled, and manipulated in real time. Some of the quantum information aspects of lateral quantum dot molecules can be found in our recent review [4]. With nanocrystals being a very active and well-covered field, in this review we will focus on self-assembled and graphene quantum dots.

The appearance of self-assembled quantum dots during the growth of InAs layers on GaAs in molecular beam epitaxy was noted as early as 1985 by Marzin and co-workers [18] and much of the pioneering work has been carried out by Petroff and co-workers [19] in the early 90's. From early theoretical and experimental research self-assembled quantum dots are finding applications in quantum dot lasers and amplifiers [20–25] and solar cells [26]. Current research, some theoretical aspects of which are reviewed in this paper, is focused on single quantum dots and quantum dot molecules with potential applications as single photon sources, sources of entangled photon pairs, and when charged, quantum bits. From a theoretical point of view these structures are challenging as they are neither few-atom molecules nor solids and involve collective behavior of millions of atoms. We will describe our attempts at providing an understanding of electronic and optical properties of million-atom nanostructures at different levels of sophistication. In particular, we will discuss to what extent the single-particle states in quantum dots can be viewed as states of two quantum harmonic oscillators. When the dots are filled with electrons, the generalized Hund's rule allows us to predict the spin of the ground state [27]. When the dots are populated with electrons and holes, as in a quantum dot laser, the hidden symmetry replaces the Hund's rule as an underlying principle governing the properties of multiexciton complexes [28–32]. The single exciton, controlling the absorption of photons by a quantum-dot-based solar cell, can be understood in terms of mixing of bright and dark configurations by Coulomb interactions [33]. Manipulating electronic and optical properties of single self-assembled quantum dots has become possible with the growth of InAs quantum dots on InP templates, pioneered by Williams and co-workers [34]. This enabled the gating of individual dots [35] and embedding of these dots in a photonic cavity [36]. These quantum dots are particularly interesting because they emit at the telecom wavelength. We will describe some of the properties of InAs/InP quantum dots using the effective bond-orbital model.

Finally, the recent isolation of a single, atomically thick carbon graphene layer [37] opened a new field of research. Since graphene does not have a gap, size quantization opens an energy gap and turns graphene into a semiconductor. Unlike in semiconductor quantum dots, the gap in graphene quantum dots can be tuned from zero to perhaps even the gap of the benzene ring. However, graphene dots need to be terminated and the edges play a very important role, with zigzag edges leading

to energy shells in the middle of the gap and a finite magnetic moment. The magnetic moment can in turn be related to another property of graphene — the sublattice symmetry. The research on graphene quantum dots is at a very early stage [38, 39] and we hope that this short review will stimulate its rapid progress.

The research field covering semiconductor and graphene quantum dots has increased tremendously since early 1990's with contributions from many outstanding scientists. It is not possible to cover the entire field and give credit to everyone in such a short article. We focus here primarily on the work carried out at the NRC Institute for Microstructural Sciences and refer the reader to existing reviews for additional coverage of the field.

2 Self-assembled quantum dots

Self-assembled quantum dots consist of a low-bandgap semiconductor A, typically InAs, embedded in a higher-bandgap semiconductor B, typically GaAs or InP [1–3]. The two materials have similar symmetry but different lattice constants. The dots are formed during the Stransky–Krastanow process of, e.g., molecular beam epitaxy of InAs on GaAs. In this process, the strain building up in the InAs layer is relieved by the formation of quasi-two-dimensional islands. The islands, typically pyramidal or lens-shaped, are capped with GaAs. An example of a lens-shaped InAs quantum dot on a wetting layer is shown in Fig. 1. When electrons and/or holes are injected into the sample, they become confined in InAs quantum dots. The remainder of this section describes the electronic properties of self-assembled quantum dots. Since the two materials are strained, we start with the effect of strain, followed by a description of electronic properties of these systems.

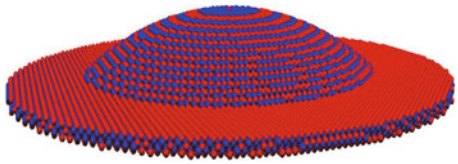

Fig. 1 Indium (*red*) and Arsenic (*blue*) atoms in a lens-shaped InAs quantum dot with diameter of 25 nm and height of 3.5 nm on a 0.6 nm high wetting layer. The GaAs barrier material atoms are not shown.

2.1 Strain distribution

As aforementioned, self-assembled quantum dots are formed to relax the strain due to the lattice mismatch between two materials grown on top of each other, like InAs/GaAs, InAs/InP or CdTe/ZnTe. The strain distribution in the vicinity of a quantum dot can be determined by either the continuum elasticity theory or the atomistic valence-force-field approach [40, 41]. The domain of strain calculation is typically a rectangular computational box which generally includes the entire structure, with characteristic sizes on the micrometer scale. Depending on the device configuration, fixed or free-standing boundary conditions are implemented [42].

In the framework of the continuum elasticity theory, the strain tensor ε is defined for each unit cell of the structure as

$$\varepsilon_{jk} = \frac{1}{2}\left(\frac{\partial u_j}{\partial r_k} + \frac{\partial u_k}{\partial r_j}\right) \tag{1}$$

where r_j and u_k are the components of the position vector $\boldsymbol{r}$ and displacement vector $\boldsymbol{u}$, respectively. It can be obtained by minimizing the following elastic energy functional:

$$\begin{aligned} E = \frac{1}{2}\int \Big[& C_{11}\left(\varepsilon_{xx}^2 + \varepsilon_{yy}^2 + \varepsilon_{zz}^2\right) \\ & + C_{44}\left(\varepsilon_{xy}^2 + \varepsilon_{yz}^2 + \varepsilon_{zx}^2\right) \\ & + 2C_{12}\left(\varepsilon_{xx}\varepsilon_{yy} + \varepsilon_{yy}\varepsilon_{zz} + \varepsilon_{zz}\varepsilon_{xx}\right)\Big] \mathrm{d}^3\boldsymbol{r} \end{aligned} \tag{2}$$

where C_{11}, C_{44}, and C_{12} are position-dependent elastic constants, assuming the value of the quantum dot or the barrier matrix materials, respectively.

In the atomistic approach, the elastic energy of each atom i is a function of the positions of its nearest neighbors,

$$\begin{aligned} E_i = & \frac{1}{2}\sum_{j=1}^{4} \frac{\alpha_{ij}}{d_{ij}^2} \cdot (\boldsymbol{R}_{ij}^2 - d_{ij}^2)^2 \\ & + \sum_{j=1}^{3}\sum_{k=j+1}^{4} \frac{\sqrt{\beta_{ij}\beta_{ik}}}{d_{ij}d_{ik}} \left(\boldsymbol{R}_{ij}\cdot\boldsymbol{R}_{ik} + \frac{1}{3}d_{ij}d_{ik}\right)^2 \end{aligned} \tag{3}$$

with d_{ij} being the bond length, and α_{ij} and β_{ij} the force constants between atoms i and j. By minimizing the total elastic energy which is a sum over all atoms, the equilibrium positions of all the atoms are computed and the corresponding strain tensor can therefore be obtained [41].

The minimization procedure can proceed either via the standard conjugate gradient method, or by a more intuitive force-field approach. As the strain energy is a function of the positions of all the unit cells or atoms, i.e., $E = E(\boldsymbol{r}_1, \boldsymbol{r}_2, \cdots)$, the force exerted on each unit is therefore given by $\boldsymbol{F}_i = -\partial E/\partial \boldsymbol{r}_i$. In one iteration, each unit is displaced proportionally to $\boldsymbol{F}_i$. The iterative procedure ends when the amplitudes of all the forces become sufficiently small. In zinc-blende semiconductors such as InAs or GaAs, shear strain would induce piezoelectric charge along the interface between neighboring unit cells [42], as given by

$$\rho_P(\boldsymbol{r}) = -2e_{14}\left[\frac{\partial\varepsilon_{yz}(\boldsymbol{r})}{\partial x} + \frac{\partial\varepsilon_{xz}(\boldsymbol{r})}{\partial y} + \frac{\partial\varepsilon_{xy}(\boldsymbol{r})}{\partial x}\right] \tag{4}$$

The piezoelectric potential can be obtained by solving the corresponding Poisson equation.

In Table 1 we list the elastic constants (in unit of 10^{11} dyne/cm^{-1}), piezoelectric modulus (C·m^{-2}), ideal bond lengths (Å) and force constants (10^3 dyne) of InAs, GaAs and InP. Figure 2 shows the shear strain component ε_{xy} and piezoelectric potential calculated for a lens-shaped InAs/GaAs self-assembled quantum dot with a base diameter of 19.8 nm and a height of 2.8 nm placed on a two-monolayer wetting layer (ML). Red/blue area corresponds to positive/negative part of the strain and potential.

Table 1 List of material parameters used in the strain calculation by the continuum or atomistic elasticity theory.

	InAs	GaAs	InP
C_{11}	8.329	11.879	10.22
C_{12}	4.526	5.376	5.76
C_{44}	3.96	5.94	4.6
e_{14}	0.045	0.16	0.035
d	2.622	2.448	2.537
α	35.18	41.19	43.04
β	5.50	8.95	6.24

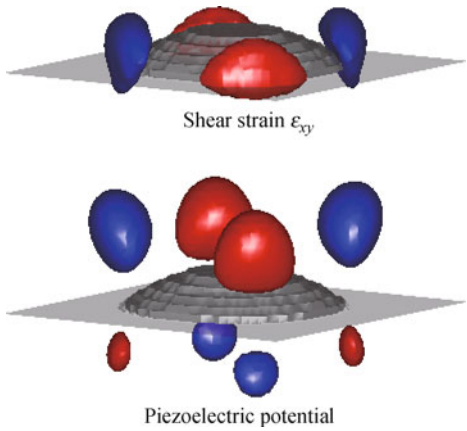

Fig. 2 Isosurface plots of the shear strain component ε_{xy} and piezoelectric potential in a lens-shaped InAs/GaAs self-assembled quantum dot.

2.2 Electronic structure

Within the framework of continuum elasticity, the effect of strain on the electronic structure of a self-assembled quantum dot is described by the Bir–Pikus deformation potential theory [43]. There are two major components of the strain which modifies the band-edge energies, the hydrostatic (H_s) and the biaxial (B_s), as defined in the following:

$$H_s = \varepsilon_{xx} + \varepsilon_{yy} + \varepsilon_{zz}$$
$$B_s^2 = (\varepsilon_{xx} - \varepsilon_{yy})^2 + (\varepsilon_{yy} - \varepsilon_{zz})^2 + (\varepsilon_{zz} - \varepsilon_{xx})^2 \quad (5)$$

The band-edge energies of the conduction bands are mainly affected by the hydrostatic component of the strain while the heavy- and light-hole bands are further influenced by the biaxial strain components, i.e.,

$$U_c = a_c H_s + E_{bo}^c$$
$$U_{hh} = -a_v H_s - b_v B_s + E_{bo}^v$$
$$U_{lh} = -a_v H_s + b_v B_s + E_{bo}^v \quad (6)$$

where E_{bo}^c and E_{bo}^v are the band offsets between the dot and matrix materials before strain, and a_c, a_v, and b_v are the deformation potential parameters [40].

Figure 3 plots the confining potentials for electrons, heavy- and light-holes along the growth direction (upper panel) and along the diameter of the bottom base of the dot. The height of the dot is chosen to be the same as that in Fig. 2 while the diameter is twice as large for better visualization. It is seen that the effective band-gap in the presence of the strain is increased to about 695 meV from 475 meV in the strain free bulk InAs. The strain is also seen to enhance the depth of the confining potential for the heavy-holes to about 300 meV from 85 meV. The heavy- and light-hole bands which are degenerate in the bulk are now lifted by the biaxial strain component. The splitting in the middle of the dot is about 177 meV.

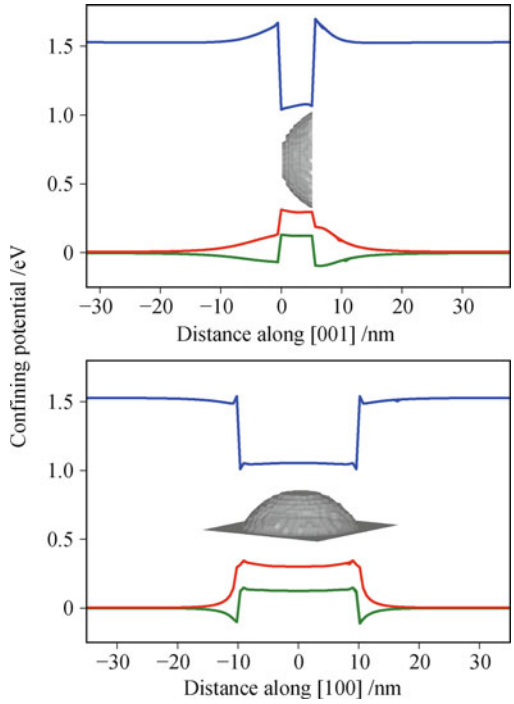

Fig. 3 Confining potentials for electrons, heavy- and light-holes (from top to bottom) deformed by the strain InAs/GaAs self-assembled quantum dot.

Besides the effect on the band-edge energies, the strain also modifies the effective masses of electrons and holes in the dot.

2.2.1 Effective-mass approximation

The states confined in the quantum dot are often composed of components from both the conduction and valence bands. With the biaxial strain present in the self-assembled quantum dots, the degeneracy between the heavy and light holes is lifted and the low-lying states in the valence band have mostly a heavy hole character.

If the effect of band mixing between the conduction and valence bands is neglected, the problem could be reduced to two separate single-band effective-mass equations, one for electron and the other for hole, as given by [44]

$$\hat{H}_e = -\frac{\hbar^2}{2m_e^{//}}\left(\frac{\partial^2}{\partial x^2}+\frac{\partial^2}{\partial y^2}\right)-\frac{\hbar^2}{2m_e^{\perp}}\frac{\partial^2}{\partial z^2}+U_c+V_p$$
$$\hat{H}_h = \frac{\hbar^2}{2m_h^{//}}\left(\frac{\partial^2}{\partial x^2}+\frac{\partial^2}{\partial y^2}\right)+\frac{\hbar^2}{2m_h^{\perp}}\frac{\partial^2}{\partial z^2}+U_{hh}-V_p \quad (7)$$

where V_p is the piezoelectric potential. Although the electron effective mass is almost isotropic in most III–V semiconductors, two independent components, $m_e^{//}$ and $m_e^{\perp}$, are used to reflect the anisotropic geometries of the quantum dots, and so are the analogous masses for holes.

Since there is no a priori rule on how to choose the effective masses within the model itself, $m_e^{//}$, $m_e^{\perp}$, $m_h^{//}$, and $m_h^{\perp}$ are treated as adjustable parameters which are determined by fitting the calculated energy spectrum to that obtained by a more sophisticated approach like the multiband $\boldsymbol{k}\cdot\boldsymbol{p}$ or the empirical tight-binding method described below. A way to avoid the fitting procedure is to regard the effective masses as position-dependent variables [45].

It is found that the electron effective mass in quantum dots is generally larger than the bulk value and becomes anisotropic in the dots of large aspect ratio between the vertical and lateral dimensions. Unlike the bulk material, the hole effective mass is seen to be almost isotropic in the dots of small aspect ratio. For an example of flat InAs/GaAs quantum dots, the most appropriate value for the electron and hole effective mass is believed to be the electron effective mass in bulk GaAs (0.067 m_0) and the vertical heavy-hole effective mass in bulk InAs (0.34 m_0), respectively.

2.2.2 *Parabolic confinement model*

The effective mass model has been applied to lens-shaped quantum dots [46]. It was shown that, in the adiabatic approximation, the radial confining potentials for electrons and heavy holes can be well approximated by parabolas with a given depth and radius of the dot. The single-electron Hamiltonian is reduced to a Hamiltonian of two bosons, two 1D harmonic oscillators (HOs) with creation (annihilation) operators $a_m^+(a_m)$ and energy level spacing $\hbar\omega_e$ [7],

$$\hat{H}_{ho} = \hbar\omega_e\left(m+\frac{1}{2}\right)a_m^+a_m+\hbar\omega_e\left(n+\frac{1}{2}\right)a_n^+a_n \quad (8)$$

The corresponding wave functions are those of the two-dimensional harmonic oscillator. A similar model is applied to heavy holes, and the analytical solution for HO states in a perpendicular magnetic field can be found, e.g., in Ref. [7]. It was recently demonstrated that InAs/InP and disk-like InAs/GaAs dots grown using the indium-flush technique developed by Wasilewski and coworkers [47] can be well described by the HO model. If the HO states are populated by photoexcited electrons and holes with increasing excitation power, as illustrated in Fig. 4(c), the resulting emission spectrum consists of several peaks corresponding to electron and hole shells. The evolution of the emission spectrum with an increasing magnetic field is shown in Figs. 4(a) and (b). The spectrum strikingly resembles that of the 2D HO in a magnetic field. As already mentioned, the HO model works quite well, but the parameters of the model, masses, and confinement energies $\hbar\omega_e$ and $\hbar\omega_h$ are fitting parameters that must be obtained by other methods like the multiband $\boldsymbol{k}\cdot\boldsymbol{p}$ or empirical tight-binding method described below.

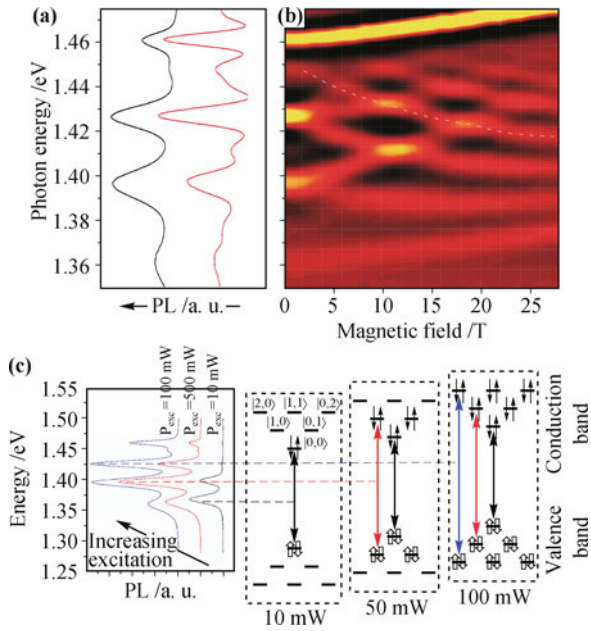

Fig. 4 Emission spectrum of an ensemble of InAs/GaAs self-assembled quantum dots as a function of applied magnetic field shows harmonic oscillator states. Reproduced from Ref. [48], Copyright © 2004 American Physical Society.

2.2.3 *Eight-band $\boldsymbol{k}\cdot\boldsymbol{p}$ approach*

The eight-band $\boldsymbol{k}\cdot\boldsymbol{p}$ method uses eight Bloch functions at the Γ point of the Brillouin zone as the basis functions to describe electron states with a finite wave vector. As the lateral size of quantum dots is usually much larger than the lattice constant, the $\boldsymbol{k}\cdot\boldsymbol{p}$ method has been widely used in the calculation of confined electron states. In general, the multiband $\boldsymbol{k}\cdot\boldsymbol{p}$ Hamiltonian can be written as

$$\begin{aligned}\hat{H}_{\boldsymbol{k}\cdot\boldsymbol{p}} = {} & \boldsymbol{E}_{bo}+\boldsymbol{A}_x\hat{k}_x\hat{k}_x+\boldsymbol{A}_y\hat{k}_y\hat{k}_y+\boldsymbol{A}_z\hat{k}_z\hat{k}_z \\ & +\boldsymbol{B}_{xy}\hat{k}_x\hat{k}_y+\boldsymbol{B}_{yz}\hat{k}_y\hat{k}_z+\boldsymbol{B}_{xz}\hat{k}_x\hat{k}_z \\ & +\boldsymbol{C}_x\hat{k}_x+\boldsymbol{C}_y\hat{k}_y+\boldsymbol{C}_z\hat{k}_z+V_P \end{aligned} \quad (9)$$

where $\boldsymbol{E}_{bo}$ is the matrix for the band offsets, and $\boldsymbol{A}$, $\boldsymbol{B}$, and $\boldsymbol{C}$ are the matrices of coefficients [49]. Within the deformation potential theory, an additional part $\hat{H}_s$, which has a similar structure as $\hat{H}_{\boldsymbol{k}\cdot\boldsymbol{p}}$, is added to take into account the effects due to strain [50]. The computational box for the calculation of the electronic structure of quantum dots is not necessarily as large as that used for the strain since the confined states are mostly localized inside the quantum dots. The Hamiltonian is first discretized on a reduced three-dimensional mesh, which results in a large, sparse matrix, and then is diagonalized by utilizing the Lanczos algorithm [51].

The wave function of a single-particle state, ψ, is the sum of products of envelope functions $\phi_k(\boldsymbol{r})$ and basis functions $u_k(\boldsymbol{r})$, i.e., $\psi(\boldsymbol{r}) = \sum_n \phi_n(\boldsymbol{r})u_n(\boldsymbol{r})$. The basis functions are usually taken as $|s\rangle$, $|x\rangle$, $|y\rangle$, and $|z\rangle$, coupled with two eigenspinors $|\uparrow\rangle$ and $|\downarrow\rangle$. These functions are referred to as the uncoupled spin–orbital basis. Because of the spin–orbit interaction, only the total angular momentum is a good quantum number. Therefore, the eigenfunctions of the total angular momentum operator are considered to be a more convenient choice of what is referred to as the coupled spin–orbital basis. These basis functions are closer to the band-edge Bloch functions than the uncoupled set. Note that the coefficient matrices in the $\boldsymbol{k}\cdot\boldsymbol{p}$ Hamiltonian take different forms in the uncoupled and coupled spin–orbital basis [52].

Figure 5 shows the density of states for a lens-shaped InAs/GaAs self-assembled quantum dot grown on a 2 ML wetting layer with a base diameter of 25.4 nm and a height of 2.8 nm. The confined states in the conduction bands are seen to form almost equally spaced clusters, with increasing number of states in each one, in analogy to the HO model. The density of states in the valence band is found to increase steadily as the energy approaches the continuum. Figure 5 also shows the composition of the states, i.e., the proportion of each kind of components. It is seen that the states in the conduction band are dominated by the components from the same band, however with decreasing proportion as the energy increases. In the valence band, the low-lying states are found to be dominated by the heavy-hole components, while the proportion of the light-hole components is non-negligible in high-lying states. Close to the continuum, the proportion of the heavy- and light-hole components is seen to be saturated at around 60% and 25%, respectively.

Since the eight-band $\boldsymbol{k}\cdot\boldsymbol{p}$ method keeps a good balance between handling complicated band mixing effects and computational complexity, it has become widely used in the calculation of the electronic structure of self-assembled quantum dots, and successfully explained many interesting phenomena, such as inverted electron-hole alignment in intermixed single quantum dots [53] and spontaneous localization of hole states in

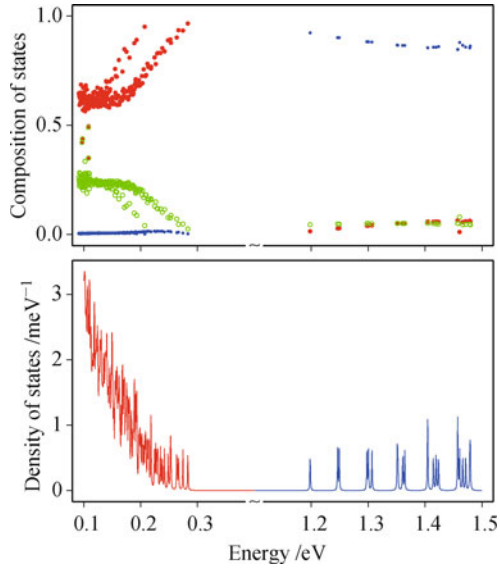

Fig. 5 Density of states (lower panel) and composition of states (upper panel) calculated for a lens-shaped InAs/GaAs self-assembled quantum dot. Small solid dots (blue) are for the components from the conduction bands, larger ones (red) for the heavy-hole components, and open dots (green) for the light-hole components.

quantum-dot molecules [54]. The $\boldsymbol{k}\cdot\boldsymbol{p}$ method predicted the transition between bonding and anti-bonding states as ground states of a valence hole in a vertical quantum dot molecule as a function of the separation between the constituent quantum dots [55, 56]. This unusual behavior related to strong spin–orbit coupling was recently observed experimentally by Doty *et al.* [57].

2.2.4 Effective bond-orbital model

The multiband $\boldsymbol{k}\cdot\boldsymbol{p}$ method accounts for the proper structure of the valence band, including heavy, light, and spin split-off hole subbands. It is, however, limited to the vicinity of the Γ point, and therefore is expected to break down as the size of the nanostructure decreases. The effective bond-orbital model (EBOM) [58] is an empirical sp^3 tight-binding method in which indium-arsenic dimers are replaced by an effective atom. Hence the full symmetry of the zinc-blende lattice is reduced to that of a fcc lattice. Although EBOM misses the lack of inversion symmetry of zinc-blende structures and the microscopic atomic structure of the unit cell, it can, however, reproduce the effective masses of electrons and holes at the Γ point, as well as conduction and valence band edges at both the Γ and X points with the second nearest-neighbor interactions included [59]. The tight-binding Hamiltonian matrix describing hopping between effective s and p orbitals of effective atoms on sites $\boldsymbol{R}$ is given by

$$H(\boldsymbol{R}_{s\sigma}, \boldsymbol{R}'_{s\sigma}) = E_{ss}^{000}\delta_{\boldsymbol{R},\boldsymbol{R}'} + E_{ss}^{110}\delta_{\Delta\boldsymbol{R},\tau} + E_{ss}^{200}\delta_{\Delta\boldsymbol{R},\lambda}$$
$$H(\boldsymbol{R}_{p\sigma}, \boldsymbol{R}'_{p\sigma}) = \delta_{\Delta\boldsymbol{R},\tau}\left[E_{xx}^{110}\tau_p^2 + E_{xx}^{011}(1-\tau_p^2)\right] + \delta_{\Delta\boldsymbol{R},\lambda}\left[E_{xx}^{200}\sigma_p^2 + E_{xx}^{002}(1-\sigma_p^2)\right]$$

$$+E_{xx}^{000}\delta_{\boldsymbol{R},\boldsymbol{R}'}$$
$$H(\boldsymbol{R}_{s\sigma},\boldsymbol{R}'_{p\sigma}) = E_{sx}^{110}\tau_p\delta_{\Delta\boldsymbol{R},\tau}$$
$$H(\boldsymbol{R}_{p\sigma},\boldsymbol{R}'_{p'\sigma}) = E_{xy}^{110}\tau_p\tau_{p'}\delta_{\Delta\boldsymbol{R},\tau} \quad (10)$$

with $\Delta\boldsymbol{R} = \boldsymbol{R} - \boldsymbol{R}'$, and

$$\tau = \frac{a}{2}\big[(\pm1,\pm1,0),(\pm1,0,\pm1),(0,\pm1,\pm1)\big]$$
$$\sigma = a\big[(\pm1,0,0),(0,\pm1,0),(0,0,\pm1)\big] \quad (11)$$

being the positions of the nearest and next-nearest neighbors, respectively. The effect of strain is incorporated through the deformation potential theory and through the piezoelectric effect [60]. Table 2 shows the next-nearest-neighbor parameters for GaAs and InAs.

Table 2 Next-nearest-neighbor parameters (in eV).

	GaAs	InAs
E_{ss}^{000}	3.581011	2.698585
E_{ss}^{110}	−0.039499	−0.124187
E_{ss}^{200}	−0.264835	−0.118389
E_{sx}^{110}	0.387077	0.368502
E_{xx}^{000}	−3.301012	−3.068847
E_{xx}^{110}	0.424999	0.412500
E_{xx}^{011}	−0.070000	−0.112499
E_{xx}^{200}	−0.186297	−0.156340
E_{xx}^{002}	0.138401	0.154132
E_{xy}^{110}	0.495000	0.525000

The matrix elements for spin-orbit interaction are given by $H(\boldsymbol{R}_{x\uparrow},\boldsymbol{R}_{y\uparrow}) = -\mathrm{i}\Delta/3$, $H(\boldsymbol{R}_{x\downarrow},\boldsymbol{R}_{y\downarrow}) = \mathrm{i}\Delta/3$, $H(\boldsymbol{R}_{x\uparrow},\boldsymbol{R}_{z\downarrow}) = \Delta/3$, $H(\boldsymbol{R}_{y\uparrow},\boldsymbol{R}_{z\downarrow}) = -\mathrm{i}\Delta/3$, and their conjugate terms, with Δ being the spin-orbit splitting in the valence band. When the spin-orbit interaction is not very strong, it is possible to separate the components of an envelope function into two groups. One group consists of components for spin up basis functions, $|s_\uparrow\rangle$, $|x_\uparrow\rangle$, $|y_\uparrow\rangle$, and $|z_\uparrow\rangle$, and the other one consists of components for spin down basis functions. A pseudospin can be assigned to a state ψ if its polarization, defined as

$$p = \int |\phi_{s\uparrow}(\boldsymbol{r})|^2 + |\phi_{x\uparrow}(\boldsymbol{r})|^2 + |\phi_{y\uparrow}(\boldsymbol{r})|^2 + |\phi_{z\uparrow}(\boldsymbol{r})|^2 \,\mathrm{d}\boldsymbol{r} \quad (12)$$

is either $p \approx 1$ (a "spin" up state) or $p \approx 0$ (a "spin" down state). The assignment of pseudospin can be carried out by introducing a small magnetic field (≈ 1 mT) along the growth direction of the quantum dots to lift the degeneracy induced by the time-reversal symmetry.

2.2.5 Empirical tight-binding method

In the empirical tight-binding method we first expand the wave function in the basis of atomic orbitals

$$\phi = \sum_{\vec{R},\alpha} c_{\vec{R}\alpha}|\boldsymbol{R}\alpha\rangle \quad (13)$$

and next form the Hamiltonian matrix in this atomic basis [61]. The matrix elements are treated as parameters determined by comparison with ab-initio and/or experimental results for bulk materials. Significant amount of work has been devoted to ab-initio determination of valence and conduction bands, effective masses and band offsets for strained materials of quantum dot and barrier materials [62, 63].

By comparison, in the pseudopotential approach [64, 67], the self-consistent potential seen by an electron in a bulk material is replaced by a sum of effective atomic potentials. These atomic potentials are next used to generate the one-electron potential of the nanostructure.

In our tight-binding approach [61] the wave function on each atom is described by ten valence orbitals for each spin: one of type s, three of type p, five of type d, and an additional s^* orbital accounting for higher-lying states. Each orbital is doubly spin-degenerate, thus resulting in a total of 20 bands. The resulting Hamiltonian of a quasiparticle in an N-atom quantum dot, written in the language of second quantization, is

$$\hat{H}_{TB} = \sum_{i=1}^{N}\sum_{\alpha=1}^{20}\epsilon_{i\alpha}c_{i\alpha}^{+}c_{i\alpha} + \sum_{i=1}^{N}\sum_{\alpha=1,\beta=1}^{20}\lambda_{i\alpha,\beta}c_{i\alpha}^{+}c_{i\beta} + \sum_{i=1}^{N}\sum_{j=1}^{4}\sum_{\alpha,\beta=1}^{20}t_{i\alpha,j\beta}c_{i\alpha}^{+}c_{j\beta} \quad (14)$$

where $c_{i\alpha}^{+}$ ($c_{i\alpha}$) is the creation (annihilation) operator of a carrier on the orbital α localized on the site i, $\epsilon_{i\alpha}$ is the corresponding on-site energy; and $t_{i\alpha,j\beta}$ describes the hopping of the particle between orbitals on neighboring sites. Coupling to farther neighbors is neglected. Finally, $\lambda_{i\alpha,\beta}$ accounts for the spin–orbit interaction by introducing finite matrix elements Δ connecting p orbitals of opposite spin, residing on the same atom, following the description given by Chadi [68]. For example, $\langle p_y,\uparrow|H|\downarrow,p_z\rangle = -\mathrm{i}\Delta/3$. Spin–orbit-type coupling between d orbitals is neglected. Here we assume that each site holds 20 orbitals and is surrounded by 4 neighbors.

Hopping, i.e., off-diagonal matrix elements of our Hamiltonian are calculated according to the recipe given by Slater and Koster [69]. In this approach, the hopping matrix elements $t_{i\alpha,j\beta}$ are expressed as geometric functions of two-center integrals and depend only on the relative positions of the atoms i and j. Contributions from three-center and higher integrals are neglected. For example, if the two atoms are connected by a bond along the x axis, then orbitals s and p_z create a π bond and the matrix element $t_{s,p_z} = V_{s,p_z\pi} = 0$ vanishes because of the symmetry. On the other hand, if the direction of the bond is along y axis, then the bond is of a σ type and $t_{s,p_z} = V_{s,p_z\sigma}$ is finite. In the general case the nearest neighbors are connected by bonds of any direction $\boldsymbol{d} = |d|(l\hat{x} + m\hat{y} + n\hat{z})$, with d being the bond length

and l, m, n — the direction cosines. Then the tunneling t_{s,p_z} element can be expressed in terms of projecting the p_z orbital onto the bond and in the direction perpendicular to it. Since the perpendicular projections give π-type bonds, their contribution is zero. The Hamiltonian matrix element is thus $t_{i,s,j,p_z} = nV_{sp\sigma}$. Similar sets of rules are defined for all other t matrix elements [69]. This approach reduces the number of unknown matrix elements as they can be related via Slater–Koster rules to a relatively small subset of two-center integrals $V_{\alpha\beta,\gamma}$. This is particularly useful within the framework of empirical tight binding, where E_α, $\lambda_{\alpha,\beta}$ and $V_{\alpha\beta,\gamma}$ parameters are not directly calculated, but rather obtained by fitting the TB bulk model results to experimentally known band gaps and effective masses at high symmetry points of the Brillouin zone [70]. We stress here that we have been fitting the TB model not only to bulk properties at Γ point, but also at X and L points to account for multivalley couplings.

The TB parametrization used so far are given, e.g., in Refs. [71–73], where it was demonstrated that the inclusion of d orbitals in the basis allows to obtain much better fits of the masses and energy gaps to the target material values. In particular, the treatment of the conduction band edge is significantly improved, which is important for small nanostructures [74]. In this work we use our own parametrization, analogous to work by Klimeck *et al.* [72], but giving a better agreement with target bulk properties. More details will be presented in our future work.

In order to address the treatment of the interface between InAs and GaAs we note that these two materials share the same anion (Arsenic). Thus during the fitting procedure the diagonal matrix elements on arsenic are kept the same in both materials. This approach removes the necessity of averaging on-site matrix elements for interface atoms. Additionally, to account for the band offset (BO) between the materials forming the interface, the fit for InAs is performed in such a way that the top of the valence band of InAs is set to be equal to the BO value relative to the GaAs. This removes the necessity of shifting values of diagonal matrix element for interface atoms, which would result in two different sets of parameters for Arsenic: one for InAs and another for GaAs.

Finally, there is the second type of interface that arises on the edges of the computational box. Here, the appearance of free surfaces leads to the existence of dangling bonds. Their presence results in spurious surface states, with energy inside the gap of the barrier material, making it difficult to distinguish spurious states from the single-particle states of the quantum dot. An energy shift for dangling bonds that mimics the passivation procedure, described in Ref. [75], is performed in order to move the energies of surface-localized states away from the energies corresponding to confined quantum-dot states.

Then, a parallel Lanczos diagonalizer is used to resolve the Kramers-degenerate doublets. Because the computational domain necessary for the converged tight-binding calculation involves the order of ≈ 1 million atoms, the resulting tight-binding matrices are very large, i.e., ≈ 20 million by 20 million. This presents a significant numerical problem, but utilizing matrix sparsity, parallel computation paradigm, and the fact that we need only several lowest electron and hole states rather than the entire eigenspectrum of the Hamiltonian, we achieve linear scaling of the computational resources as a function of the number of atoms.

To illustrate the application of the different methods, we show in Fig. 6 the results of calculation for the same dot obtained with the effective bond-orbital method (labeled as EBOM), the tight-binding (TB) model, and the empirical pseudopotential method (EMP). The input parameters in EBOM and TB calculations are chosen to be similar to the ones used in empirical pseudopotential calculations (EMP1) from Ref. [64]. Another empirical pseudopotential calculation (EMP2) is shown for comparison [65]. As expected, the structure of electron states is similar in all cases, however, the hole states differ significantly. EBOM maintains approximately a shell-like structure of hole levels. This differs from both TB and EMP and can be attributed to the replacement of zinc-blende with cubic symmetry in EBOM. There is a good agreement between TB and EMP1 calculation, with a characteristic "large/large/small" level spacing between subsequent hole levels $h_1 - h_2 \approx h_2 - h_3 \gg h_3 - h_4$. Surprisingly, two pseudopotential (EMP1/EMP2) calculations predict different details of hole levels, most

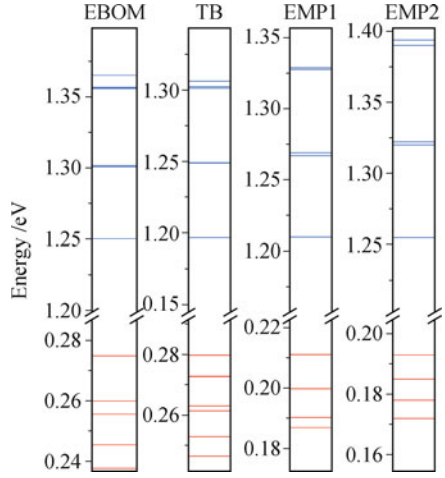

Fig. 6 Electron (blue/upper) and hole (red/lower) single-particle energies calculated for effective bond-orbital method (EBOM) and tight-binding (TB) model. The parameters of the TB model were chosen to be similar to empirical pseudopotential calculation from [64]; results of this calculation are shown as EMP1. Another empirical pseudopotential calculation (EMP2) is shown for comparison [65]. Reproduced from Ref. [61], Copyright © 2010 American Physical Society.

likely due to a slightly different choice of fitting parameters or fitted results in pseudopotential fitting procedure. More specifically, due to the insufficient number of fitting parameters, the pseudopotentials used in the EMP calculations give effective masses of GaAs and InAs off from the experimental values by more than 30% [60]. Consequently, the separations among the energy levels in the valence bands calculated by both EBOM and TB are different from those by EMP. Overall there is a good agreement between EBOM, the tight-binding and empirical pseudopotential models.

2.3 Optical properties

2.3.1 Photoluminescence: Polarization and anisotropy

Let us begin our discussion with the EBOM model and first temporarily neglect the electron–electron interaction. The momentum matrix element between an electron state $\psi_e = \sum \phi_n^e u_n$ and a hole state $\psi_h = \sum \phi_n^h u_n$ along the polarization direction $\boldsymbol{e}$ is given by

$$\langle \psi_h | \boldsymbol{e} \cdot \hat{\boldsymbol{p}} | \psi_e \rangle = \sum_{mn} \langle u_n | \boldsymbol{e} \cdot \hat{\boldsymbol{p}} | u_m \rangle \langle \phi_n^h | \phi_m^e \rangle + \sum_m \langle \phi_m^h | \boldsymbol{e} \cdot \hat{\boldsymbol{p}} | \phi_m^e \rangle \tag{15}$$

If we neglect the contribution from the envelope-function part of the wave function [76], this element can be further simplified as

$$\begin{aligned} \langle \psi_h | \hat{p}_x | \psi_e \rangle &= \mathrm{i}P_0 \cdot \left[\langle \phi_{x\uparrow}^h | \phi_{s\uparrow}^e \rangle + \langle \phi_{x\downarrow}^h | \phi_{s\downarrow}^e \rangle \right. \\ &\quad \left. - \langle \phi_{s\uparrow}^h | \phi_{x\uparrow}^e \rangle - \langle \phi_{s\downarrow}^h | \phi_{x\downarrow}^e \rangle \right] \\ \langle \psi_h | \hat{p}_y | \psi_e \rangle &= \mathrm{i}P_0 \cdot \left[\langle \phi_{y\uparrow}^h | \phi_{s\uparrow}^e \rangle + \langle \phi_{y\downarrow}^h | \phi_{s\downarrow}^e \rangle \right. \\ &\quad \left. - \langle \phi_{s\uparrow}^h | \phi_{y\uparrow}^e \rangle - \langle \phi_{s\downarrow}^h | \phi_{y\downarrow}^e \rangle \right] \end{aligned} \tag{16}$$

where $\mathrm{i}P_0 = \langle s | \hat{p}_x | x \rangle = \langle s | \hat{p}_y | y \rangle$ denotes the coupling between the conduction and valence bands. For circular polarization σ^+ or σ^-, the momentum matrix element is then given by $p_{he}^{\pm} = \left[\langle \psi_h | \hat{p}_x | \psi_e \rangle \mp \mathrm{i} \langle \psi_h | \hat{p}_y | \psi_e \rangle \right] / \sqrt{2}$. It is straightforward to show that $p_{he}^- = p_{he}^+$ in the absence of the magnetic field.

Figure 7 gives a schematic view of interband transition in an elongated quantum dot. The emission is found to be partially polarized, which is regarded to be related to the structural anisotropy [77]. The degree of linear polarization of interband transitions is then defined by

$$P_{eh} = \frac{|\langle \psi_e | \hat{p}_x | \psi_h \rangle|^2 - |\langle \psi_e | \hat{p}_y | \psi_h \rangle|^2}{|\langle \psi_e | \hat{p}_x | \psi_h \rangle|^2 + |\langle \psi_e | \hat{p}_y | \psi_h \rangle|^2} \tag{17}$$

which is found to be closely related to the polarization of envelope functions as given by [78]

$$P_{ef} = \frac{|\langle \phi_x^h | \phi_x^h \rangle|^2 - |\langle \phi_y^h | \phi_y^h \rangle|^2}{|\langle \phi_x^h | \phi_x^h \rangle|^2 + |\langle \phi_y^h | \phi_y^h \rangle|^2} \tag{18}$$

For the ground hole state in a quantum dot elongated along the x direction, the probability of the electron in the p_x orbital is found to be larger than p_y [78]. Hence, it is this selective occupancy that leads to the optical anisotropy.

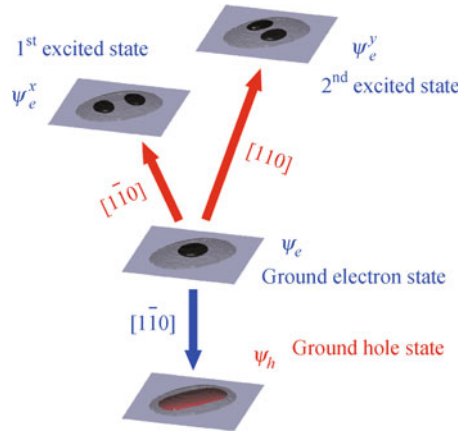

Fig. 7 Schematic view of the interband transition between the ground electronic state ψ_e and hole state ψ_h and the intersubband transitions from ψ_e to the first two excited states ψ_e^x and ψ_e^y in a quantum dot elongated along the $x = [1\bar{1}0]$ direction.

Figure 7 also shows two intersubband transitions from the ground electronic state. These transitions are polarized along the long and short axes of the structure. In a traditional single-band picture, it is trivial to find that the intersubband transitions from the ground state ψ_e to ψ_e^x and ψ_e^y are respectively polarized along the x and y directions due to the spatial symmetry of the states. In the presence of the mixing between the conduction and valence bands, however, the polarization of intersubband transitions becomes a non-trivial issue.

In the multiband formalism, the electronic states consist not only of components from the conduction band, but also those from the valence bands. Let us consider the expansions, $\psi_e = \sum \phi_S^k |k\rangle$, $\psi_e^x = \sum \phi_X^k |k\rangle$, and $\psi_e^y = \sum \phi_Y^k |k\rangle$ where the summation is over the basis $\{s, x, y, z\}$. The momentum matrix elements for the transitions $\psi_e \to \psi_e^x$ and $\psi_e \to \psi_e^y$ are then given by [79]

$$\begin{aligned} \langle \psi_e^x | \hat{p}_x | \psi_e \rangle &= \mathrm{i}P_0 \cdot \left[\langle \phi_X^s | \phi_S^x \rangle - \langle \phi_X^x | \phi_S^s \rangle \right] \\ \langle \psi_e^x | \hat{p}_y | \psi_e \rangle &= \mathrm{i}P_0 \cdot \left[\langle \phi_X^s | \phi_S^y \rangle - \langle \phi_X^y | \phi_S^s \rangle \right] \\ \langle \psi_e^y | \hat{p}_x | \psi_e \rangle &= \mathrm{i}P_0 \cdot \left[\langle \phi_Y^s | \phi_S^x \rangle - \langle \phi_Y^x | \phi_S^s \rangle \right] \\ \langle \psi_e^y | \hat{p}_y | \psi_e \rangle &= \mathrm{i}P_0 \cdot \left[\langle \phi_Y^s | \phi_S^y \rangle - \langle \phi_Y^y | \phi_S^s \rangle \right] \end{aligned} \tag{19}$$

Here the momentum matrix elements among the envelope functions have been shown to be much smaller than P_0 and hence are neglected. It is therefore seen that the polarization of the intersubband transitions now depends on those minor components of the electronic states, such as ψ_S^y and ψ_X^y from the valence bands in the presence of the mixing between the conduction and valence bands.

Further study has shown that the linearly polarized intersubband transitions are due to the simultaneous

vanishing of the four coupling terms, $\langle\phi_X^s|\phi_S^y\rangle$, $\langle\phi_X^y|\phi_S^s\rangle$, $\langle\phi_Y^s|\phi_S^x\rangle$, and $\langle\phi_Y^x|\phi_S^s\rangle$. The physics behind this rule can be understood in terms of directional interactions between the local atomistic orbitals [79].

Figure 8 shows the linear polarization of the primary interband transition against the aspect ratio for the dots with various lateral sizes and heights. It is seen that the linear polarization of the primary interband transition exhibits a quadratic dependence on the lateral aspect ratio (β). This dependence is also affected by other structural parameters such as the lateral size and height. More importantly, it is found that $P_{eh}(\beta)$ exhibits almost the same behavior for dots of similar aspect ratio between the lateral size and height [80]. This reveals the possibility of optical characterization of structural properties of self-assembled quantum dots.

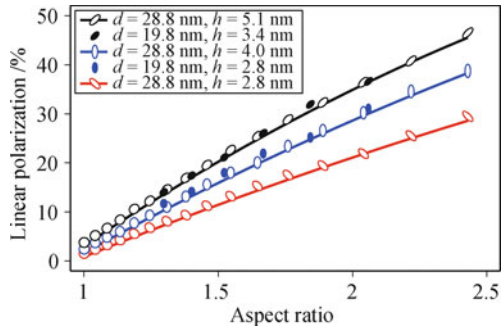

Fig. 8 Linear polarization of the primary interband transition, P_{eh} in dotted lines, calculated as a function of the aspect ratio of the quantum dots with various lateral sizes and heights. The shape and size of the symbols correspond to the denoted structures. Quadratic fit is shown in solid lines. Reproduced from Ref. [80], Copyright © 2008 American Physical Society.

2.3.2 *Electron–electron interactions and multiexciton complexes*

The absorption and emission spectra of a quantum dot are determined by an exciton, an interacting electron-hole pair. There are four exciton states, two dark and two bright. The electron–hole exchange interaction, to be discussed later, leads to the splitting of the four exciton states into a dark doublet and a bright doublet [81], and modifies the polarization of emitted photons. The emission spectra from a quantum dot with different number of excitons are different due to electron-electron interactions and this allows us to identify the emission from a single exciton, and hence the emission of a single photon. This is the principle behind the quantum dot as the single photon emitter. An emission cascade from a biexciton through two potentially indistinguishable exciton states to the quantum dot ground state leads to the emission of a pair of entangled photons [82, 83].

In a quantum-dot laser, the number of electron–hole pairs in a quantum dot increases with external excitation power. The electrons and holes interact via Coulomb interaction, and these electron–hole pairs form multiexciton complexes. A given N-exciton complex is equivalent to a specific artificial excitonic atom. An understanding of the electronic properties such as the ground state energy, total spin, total angular momentum, and emission and absorption spectra requires an understanding of the role of electron–electron and electron–hole interactions in electron–hole complexes occupying electronic shells of a quantum dot. For a given number of electron–hole pairs N the interacting Hamiltonian reads,

$$H_{ex} = \sum_i E_i^e c_i^+ c_i - \sum_i E_i^h h_i^+ h_i - \sum_{ijkl} V_{ijkl}^{he} h_i^+ c_j^+ c_k h_l + \frac{1}{2}\sum_{ijkl} V_{ijkl}^{ee} c_i^+ c_j^+ c_k c_l + \frac{1}{2}\sum_{ijkl} V_{ijkl}^{hh} h_i^+ h_j^+ h_k h_l \tag{20}$$

where E_i^e and E_i^h are the energy levels of the confined states in the conduction and valence bands, respectively. A general Coulomb matrix element is defined by

$$V_{ij,kl} = \frac{e^2}{4\pi\epsilon_0\epsilon}\int \phi_i^*(\boldsymbol{r}_1)\phi_j^*(\boldsymbol{r}_2)\frac{1}{|\boldsymbol{r}_1-\boldsymbol{r}_2|}\phi_k(\boldsymbol{r}_2)\phi_l(\boldsymbol{r}_1) \tag{21}$$

and we have $V_{ij,kl}^{ee} = V_{ij,kl}$. Note here that a confined state in the valence band ψ_h obtained from any multiband methods can be regarded as a hole state only after a conjugate transformation, $\psi_h \rightarrow \psi_h^\star$. Hence we find that $V_{ij,kl}^{hh} = V_{kl,ij}$ and $V_{ij,kl}^{he} = -V_{ik,jl}$. Once the single-particle states are obtained, the Hamiltonian for multi-excitons can be solved by the configuration–interaction method [30, 46, 61, 84].

A multiexciton complex, such as a biexciton, is composed of more than one electron–hole pair. If C_N^i is the i-th eigenstate of an N-exciton complex, its wave function can be generally written as $\Psi_N^i = \sum c_N^i|C_N^i\rangle$. Recombination of an electron–hole pair from the N-exciton complex would reduce the number of excitons to $N-1$. By taking into account every possible recombination, one can obtain the radiative lifetime, defined by

$$\frac{1}{\tau_k} = \frac{ne^2}{2\pi\varepsilon_0 m_0 c^3}\int \left[f_k^{\sigma_+}(\omega) + f_k^{\sigma_-}(\omega)\right]\omega^2 \mathrm{d}\omega \tag{22}$$

with $f_k^{\sigma_\pm}(\omega)$ being the oscillator strength,

$$f_k^{\sigma_\pm}(\omega) = \frac{2}{m_0\hbar\omega}\sum_i f(E_N^i)|c_N^i|^2 \sum_f |c_{N-1}^f|^2 \times |\langle C_{N-1}^f|P_{\sigma_\pm}^-|C_N^i\rangle|^2 \delta(E_N^i - E_{N-1}^f - \hbar\omega) \tag{23}$$

The radiative lifetime of a single exciton is typically around 1 ns. Note that the final state of the $(N-1)$-exciton complex, Ψ_{N-1}^f, may not be its ground state after the recombination of an electron–hole pair. The emission intensity is given by

$$I_N^{\sigma_\pm}(\hbar\omega) = \sum_i f(E_N^i)|c_N^i|^2 \sum_f |c_{N-1}^f|^2 \times |\langle C_{N-1}^f|P_{\sigma_\pm}^-|C_N^i\rangle|^2 \times \delta(E_N^i - E_{N-1}^f - \hbar\omega) \quad (24)$$

where the probability function $f(E_N^i)$ is given by $\exp(-E_N^i/\kappa T)/\sum_j \exp(-E_N^j/\kappa T)$ and C_N^i is the i-th eigenstate of the N-exciton system. The operator $P_{\sigma_\pm}^-$ describes all possible ways of electron–hole recombination, i.e., $P_{\sigma_\pm}^- = \sum_{nm} p_{nm}^\pm h_n c_m$. In the absence of magnetic field we have $I_N^{\sigma^+}(E) = I_N^{\sigma^-}(E)$. The emission spectrum observed in experiments is a sum of the contribution from individual multiple exciton complexes weighed by the corresponding occupation number n_k, i.e., $I(\hbar\omega) = \sum n_k I_k(\hbar\omega)$. Recent photon correlation experiments allow to untangle complicated emission spectra and extract spectra corresponding to fixed exciton numbers [85].

2.3.3 Hidden symmetry

The main difficulty with determining the ground state of the multiexciton complex exists for partially filled degenerate quantum dot states. All configurations have the same energy and there is no single configuration which dominates the ground state. Fortunately, it was shown that the fully interacting electron–hole Hamiltonian and exciton creation operator on any degenerate shell satisfies the following commutation relation: $[\hat{H}_{ex}, P^+] = E_X P^+$ where P^+ creates an exciton and E_X is a single exciton binding energy [28]. This commutation relation allows to construct exact eigenstates of the fully interacting Hamiltonian, called multiplicative states. These states are the ground states of multiexciton complexes and, as a consequence, emission from a degenerate shell takes place with energy E_X independent of the population of this shell, i.e., the number of multiexciton complexes N. This property of quantum dots is called hidden symmetry. For more information on the hidden symmetry in quantum dots we refer the reader to Refs. [28, 30, 32, 61, 84].

2.3.4 Fine structure: Electron–hole exchange interaction

Let us denote the total energy of an ideal ground state of a semiconductor, i.e., a fully occupied valence band plus an empty conduction band, as E_0. If one removes an electron from a state i in the valence band to a state j in the conduction band, the energy of the system changes to E_{ij}. If one adds an electron back to the same state in the valence band, the difference between E_{ij} and E_0 would just be the interaction energy between two electrons, one in state i and the other one in state j, i.e, $E_0 + C = E_{ij} + V_{ij,ij} - V_{ij,ji}$. Here C is the energy of interactions between the electron in the conduction band, and each electron in the valence band, and can be regarded as a constant. Hence, the energy of an electron–hole pair is given by $-V_{ij,ji} + V_{ij,ij}$ with the first term being the electron–hole direct attraction and the other one — the electron–hole exchange repulsion. In general, the matrix element for the electron–hole exchange interaction is given by

$$V_{ij,kl} = \frac{e^2}{4\pi\epsilon_0\epsilon}\int \phi_i(\boldsymbol{r}_1)\phi_j^*(\boldsymbol{r}_2)\frac{1}{|\boldsymbol{r}_1 - \boldsymbol{r}_2|}\phi_k^*(\boldsymbol{r}_2)\phi_l(\boldsymbol{r}_1) \quad (25)$$

In bulk, the electron–hole exchange interaction arises from the overlap between the s orbitals in cations, where most of the electron wave function is localized, and p orbitals in anions, accounting for most of the wave function of the hole. This also accounts for the mixing between conduction and valence bands.

The electron–hole exchange interaction is responsible for the fine structure in the optical spectra of an exciton. Without the exchange interaction, the exciton composed of an electron with spin $s = \pm 1/2$ and a heavy hole with spin $\tau = \pm 3/2$ would be four-fold degenerate. With $L = s + \tau$ as the total angular momentum, the four states form a bright doublet with $L = \pm 1$ and a dark doublet with $L = \pm 2$. The electron–hole exchange interaction splits the dark and bright doublets, with dark excitons at lower energy. Even more importantly, the bright doublet is also split into two linearly polarized exciton states by the long-range electron–hole exchange interaction. The splitting of the two exciton doublets is a function of the anisotropy of the quantum dot. Since the splitting prevents the emission of entangled photon pairs in the biexciton cascade, the theory of the fine structure of exciton has been extensively studied, e.g., by Takagahara [86, 87], Ivchenko and co-workers [88], and Kadantsev *et al.* [89] and analyzed in atomistic approaches [61, 90]. Since the fine structure splitting is on the order of tens to hundreds of μeV, cautions must be taken in extracting numbers from multi-million atom simulations. Significant effort is also devoted to controlling the exciton fine structure [91–93].

2.4 Quantum dots in magnetic fields

The effect of magnetic field has been incorporated into the EBOM Hamiltonian by introducing Peierls phase factors as follows:

$$H(\boldsymbol{R}, \boldsymbol{R}') \to \mathrm{e}^{-\mathrm{i}\frac{e}{\hbar}\int_{\boldsymbol{R}}^{\boldsymbol{R}'} \boldsymbol{A}(\boldsymbol{r})\mathrm{d}\boldsymbol{r}} \cdot H(\boldsymbol{R}, \boldsymbol{R}') \quad (26)$$

where $\boldsymbol{A}(\boldsymbol{r})$ is the vector potential. The Zeeman effect is included by adding the spin terms to the diagonal matrix elements,

$$H(\boldsymbol{R}_{\uparrow(\downarrow)}, \boldsymbol{R}_{\uparrow(\downarrow)}) \to H(\boldsymbol{R}_{\uparrow(\downarrow)}, \boldsymbol{R}_{\uparrow(\downarrow)}) \pm \frac{1}{2} g_0 \mu_B B_z \quad (27)$$

where g_0 is the g factor of a bare electron. The magnetic properties of quantum dots such as the effective electron g factors depend sensitively on the parameters used in the calculation. In the EBOM Hamiltonian all the fitting parameters are established in a closed form as a function of band edges and effective masses, and thus can be uniquely determined.

2.4.1 Multiexciton Fock–Darwin spectrum

Multiexciton complexes in quantum dots have been investigated by us in Refs. [48, 94]. As mentioned previously, the confinement for the electrons in the conduction bands in a flat quantum dot can be well approximated as a two-dimensional parabolic potential. The energy spectrum of confined electronic states is therefore the same as that of a harmonic oscillator, which is also known as the Fock–Darwin spectrum in the presence of applied magnetic field. In experiments, shown in Fig. 4, one observes the emission spectrum from multiple exciton complexes instead of the energy spectrum of single-particle states. Nevertheless, there is a correlation between the spectra of single-particle states and emission of multiple excitons. According to Koopmans' theorem for a few-particle system, it is a good approximation to treat the addition energy, $E_N - E_{N-1}$, i.e., emission energy of multiple excitons as the corresponding single-particle excitation energy, $E_n^e - E_n^h$. Hence, it is not surprising to observe Fock–Darwin-like spectra in experiments on ensemble of quantum dots [48] as well as in single dots [95].

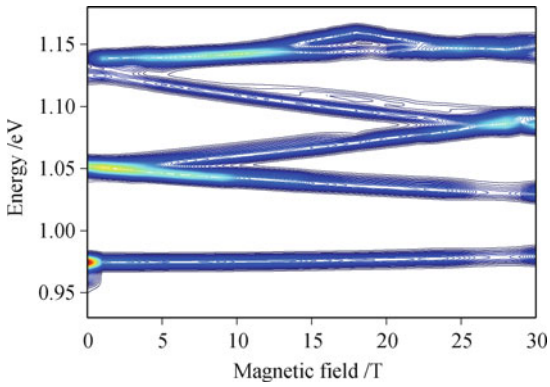

Fig. 9 Contour plot of the multiexciton emission spectrum of a lens-shaped InAs/GaAs self-assembled quantum dot.

Numerical simulation of multiexciton emission involves several steps from determination of strain distribution, calculation of the single-particle energy spectrum, computing multiexciton states by using the configuration-interaction method, solving rate equations to determine occupation of multiple exciton states to finally obtaining the emission spectrum [94]. Figure 9 shows the multiexciton emission spectrum calculated for a lens-shaped InAs/GaAs self-assembled quantum dot which is grown on a 2 ML wetting layer and has a base diameter of 19.8 nm and height of 3.4 nm. For a dot of such small lateral dimensions, the diamagnetic shift of the single exciton line is barely noticeable. However, the splitting of the two p-like states and crossing of the p and d orbitals is observed.

2.4.2 Electron g factors: Distribution and anisotropy

In bulk semiconductors such as GaAs and InAs, the electron g factor can deviate substantially from the bare electron g factor due to strong band mixing effects and the spin–orbit interaction. In turn, in self-assembled quantum dots the complicated environment like the strong quantum confinement and long-ranged strain field makes electron g factors greatly different from those in the bulk [96]. Interestingly, in InAs/GaAs self-assembled quantum dots the ensemble average value of the electron g factor does not deviate too much from that in single dots [97]. It implies that the g factors for individual islands are similar, and therefore the inhomogeneous broadening of the quantum dot size and composition does not influence the measured g factors significantly.

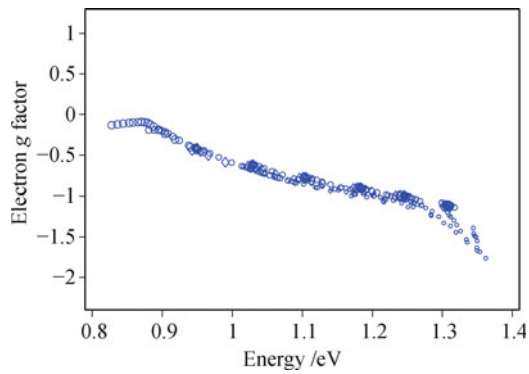

Fig. 10 Electron g factors as a function of the single exciton emission energy calculated for InAs/GaAs quantum dots with various sizes, shapes and composition profiles. Circles and diamonds stand for lens-shaped and pyramidal dots, respectively. The size of the symbols corresponds to the denoted structures.

Figure 10 shows the electron g factors calculated as a function of the emission energy for an ensemble of InAs/GaAs dots with various sizes, shapes and composition profiles [98]. For all the samples, the electron g factors are found to carry a negative sign and have magnitudes smaller than 2.0. Except for some extremely large or small samples, the electron g factors fall between -0.5 and -1.0. To understand this interesting behavior, we need to recall that an electronic state ψ_e in quantum dots, in the coupled spin–orbital basis, is composed of components from the conduction bands (s), heavy (hh), light (lh), and split-off (sh) hole subbands,

$$\psi_e = \phi_s|s\rangle + \phi_{hh}|hh\rangle + \phi_{lh}|lh\rangle + \phi_{sh}|sh\rangle \quad (28)$$

The electronic state is dominated by the s component from the conduction bands followed by the light and

heavy hole components from the valence bands. In the bulk, the holes in different bands have distinctive g factors, i.e., $g^s_{hh} = -6\kappa$, $g^s_{lh} = g^s_{sh} = -2\kappa$ where κ is an empirical parameter. In quantum dots we propose that the longitudinal electron g factor can be expressed as

$$g_e^{\perp} = 2.0 \cdot |\langle\phi_s|\phi_s\rangle|^2 - 6\kappa \cdot |\langle\phi_{hh}|\phi_{hh}\rangle|^2 - 2\kappa \cdot |\langle\phi_{lh}|\phi_{lh}\rangle|^2 - 2\kappa \cdot |\langle\phi_{sh}|\phi_{sh}\rangle|^2 \quad (29)$$

with κ now being a fitting parameter. By fitting this empirical formulation with the result from numerical calculation, we find a weak dependence of κ on the dimensions of the dots. Typically, it falls between 9.4 and 10.1. The theory therefore well explains why the fluctuation of size, shape, and even composition profile does not have much influence on the electron g factor [99].

Electron g factors are almost isotropic in bulk semiconductors such as InAs or GaAs. However, like the electron effective mass [44], they become anisotropic in self-assembled quantum dots. The in-plane electron g factor is given by

$$g_e^{//} = 2|\langle\phi_s|\phi_s\rangle|^2 + g^{//}_{lh}|\langle\phi_{lh}|\phi_{lh}\rangle|^2 + g^{//}_{sh}|\langle\phi_{sh}|\phi_{sh}\rangle|^2 \quad (30)$$

and further we have an anisotropic electron g factor [100]

$$g_e^{\perp} - g_e^{//} = -6\kappa \cdot |\langle\phi_{hh}|\phi_{hh}\rangle|^2 + 2\kappa \cdot |\langle\phi_{lh}|\phi_{lh}\rangle|^2 \quad (31)$$

As $g^{//}_{lh} = -4\kappa$ and $g^{//}_{sh} = -2\kappa$ are isotropic within the growth plane of the dots, the in-plane electron g factor remains isotropic within the lateral dimensions.

2.4.3 Hole g factors: Envelope orbital momentum

In contrast with electronic states, the valence-band states have more complicated composition structure due to strong mixing between heavy- and light-hole subbands. As these two bands have distinctive g factor tensors [see Eq. (29)], the hole states in quantum dots thus exhibit interesting behavior. Figure 11 shows the hole g factors calculated for the same set of the quantum dots as in Fig. 10. Compared with electron g factors, the hole g factors are seen to be distributed

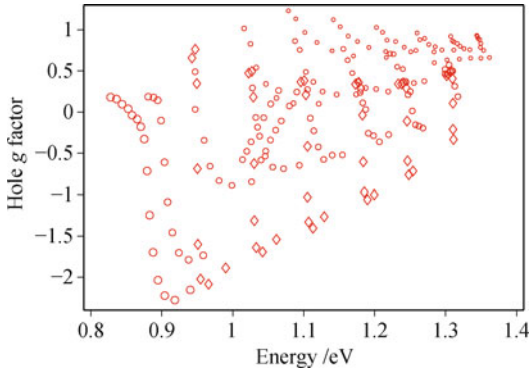

Fig. 11 Hole g factors against the single exciton emission energy calculated for the same set of InAs/GaAs quantum dots as in Fig. 10.

in more wider region, ranged from −2.5 to 1.5. Furthermore, their dependence on the emission energy is found to be more irregular.

In bulk InAs and GaAs both electron and hole g factors are negative. In InAs/GaAs quantum dots, electron g factors are found to always carry a negative sign. The reason why some dots can have positive hole g factors lies in the nonzero envelope orbital momenta (NEOM) carried by the components of the hole states [101]. Keeping in mind the expansion of any single-particle wave function as in Eq. (28), in general, one only needs to consider the contribution from the Bloch functions to the overall g factor because envelope functions usually do not carry any NEOM, and therefore have no effect on the g factor.

However, we find that the light-hole component of the ground hole states in a quantum dot does carry NEOM despite the fact that the heavy-hole part does not. The reason why the heavy hole component of a zero angular momentum can mix with the light-hole parts of nonzero angular momenta lies in the fact that the total angular momentum, i.e., that of the envelope part plus that of the Bloch part, is a good quantum number in a system with cylindrical symmetry. Even when the symmetry is broken by the shear strain, we find that the conservation of the total angular momentum is still a good approximation. Including the contribution from the envelope functions, we have the overall hole g factor

$$g_h = g^s_h + g^o_h \quad (32)$$

where g^o_h denotes the contribution from NEOM,

$$g^o_h = 2 \sum_{n\in hh,lh,sh,s} \langle\phi_{n\uparrow}|\hat{L}_z|\phi_{n\uparrow}\rangle + \langle\phi_{n\downarrow}|\hat{L}_z|\phi_{n\downarrow}\rangle \quad (33)$$

Although the light-hole component carries NEOM, its contribution to the overall g factor is small because of its small projection in the hole state. It is found that the heavy-hole part gains more and more NEOM as the height of the dot increases while the lateral dimension is fixed. If the contribution from NEOM carried by the heavy-hole component exceeds that from the Bloch part in absolute amplitude, the overall hole g factor is seen to change its sign and becomes positive. If the positive hole g factor and the negative electron g factor are similar in amplitude, the overall exciton g factor can even vanish [101].

Apart from the sign change, the hole g factor also exhibits an interesting anisotropy. As the biaxial strain in quantum dots splits the heavy and light hole apart, the low-lying states in the valence bands are dominated by their heavy-hole components (see Fig. 5). Recall that the basis functions for the heavy-hole band at the Γ point are given by $|x\uparrow\rangle + \mathrm{i}|y\uparrow\rangle$ and $|x\downarrow\rangle - \mathrm{i}|y\downarrow\rangle$, with orbital angular momenta oriented along the growth (z) direction. The spin–orbit interaction couples the spin to the orbital angular momentum and results in the z direction

being the easy-axis of polarization of total angular momentum (quasi-spin). If a hole state is composed of only the heavy-hole component, it would lead to the hole spin frozen along the growth direction and thus a zero g factor in the presence of a magnetic field applied in the growth plane [102].

For a hole state in a realistic quantum dot, its minor light-hole and split-hole components help to retain a small g factor in the Voigt configuration. Unlike an almost isotropic in-plane electron g factor [99], the in-plane hole g factor can be highly anisotropic due to NEOM carried by mainly the light-hole parts [103].

2.5 Quantum dots in electric fields

As in bulk materials and quantum wells, electronic and optical properties of self-assembled quantum dots can be probed and then tuned by applying external electric fields. The electric field can be applied either along the growth direction or in the growth plane.

2.5.1 Quantum-confined Stark effect

In the presence of an external electric field F applied along the z (growth) direction, the Hamiltonian for an electron confined in quantum dots is given by $\hat{H} + q_e F z$. For flat quantum dots with strong confinement along the vertical direction, the additional term for the electric field $q_e F z$ can usually be regarded as a perturbation. Hence the energy of the electron ground state ψ_0 in the electric field becomes

$$E_0' \approx \langle\psi_0|\hat{H}|\psi_0\rangle + q_e F\langle\psi_0|z|\psi_0\rangle + q_e^2 F^2 \sum_{n=1} \frac{\langle\psi_0|z|\psi_n\rangle\langle\psi_n|z|\psi_0\rangle}{E_0 - E_n} \quad (34)$$

with $E_0 = \langle\psi_0|\hat{H}|\psi_0\rangle$ being the energy in the absence of the field. The coefficients of the linear and quadratic terms are given by $\alpha = q_e\langle z\rangle$ and $\beta = q_e^2 \sum_{n=1} |z_{0n}|^2/\Delta E_{0n}$, respectively. Combining the formulations for electrons and holes together, we have the transition energy for an electron–hole pair given by

$$E_e' - E_h' = (E_e - E_h) + pF + \beta F^2 \quad (35)$$

where $p = q_e(\langle z_e\rangle - \langle z_h\rangle)$ is the built-in dipole moment, and $\beta = \beta_e - \beta_h$ measures the polarization of the electron and hole states. As the effect of electric field on the exciton binding energy can be approximated by a similar expansion, the above expression may also be used for the emission energy of single excitons. If there is a non-zero built-in dipole moment in the dot, the Stark shift would be asymmetric [104].

Since in the Stark shift the linear term in electric field is the electron–hole dipole moment, the information about the relative positions of the electron and hole states in the quantum dots can be determined by experiments. For a quantum dot with a homogeneous composition profile, the ground hole state is found to be localized closer to the bottom of the dot than the electron state [40]. This is due to the fact that the electron state is affected by only the hydrostatic strain while hole states are heavily influenced by the biaxial strain component. Surprisingly, an inverted electron–hole alignment was found in an experiment on the Stark effect in self-assembled quantum dots [105], which was later attributed to the inter-diffusion effect [53].

The lateral electric field has also been applied to exciton complexes in quantum dots. The two main reasons are i) attempt to modify the anisotropy of the quantum dot and hence the exciton fine structure [86, 106, 107] and ii) modification of the biexciton binding energy [35, 114]. It was shown that the electric field alone cannot remove the exciton fine structure splitting. However, the removal of the biexciton binding energy provides an alternative route to generation of entangled photon pairs without the need for the modification of quantum dot structural parameters such as anisotropy [35, 114].

2.5.2 Electrical tuning of exciton g factors

The effect of an applied electric field on a quantum dot is not limited to the Stark shift observed in the optical transitions. Other properties such as polarization of the photoluminescence emission and even exciton effective g factor may also be affected. Electrical tuning of exciton g factors in *single* [108] and *stacked* [109] InAs/GaAs quantum dots has already been demonstrated in recent experiments.

The spin splitting of an exciton state consists of the contributions from both electron and hole states, i.e., $g_x = g_e + g_h$. Although it is still very difficult to measure electron and hole g factors independently in experiment, g_e and g_h can be calculated separately. Our model system here is a pyramidal dot with a base length of b= 20 nm. Figure 12 plots the hole g factor as a function of the applied field for the dot of various height. For all the

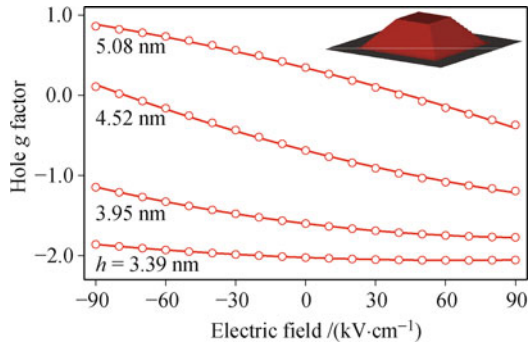

Fig. 12 Hole g factor as a function of the applied electric field for a pyramidal InAs/GaAs quantum dot of various height which is illustrated schematically in the inset.

dots, we find that electron g factor is strongly resistive to the applied electric field and exhibits very little change over a broad range of the field strength, and therefore do not show its result in the figure. On the contrary, the hole g factor is seen quite sensitive to the applied field and even changes its sign in the dots of high aspect ratio.

The g factors of electronic states are known to be insensitive to the size, geometry, and even the composition profile of the quantum dots [99]. The independence of g_e on the applied electric field can be attributed to the same physical mechanism. The hole g factor has been shown to increase with the height of the dot [101]. This dimensional dependence of the hole g factor is explained in terms of NEOM carried in the ground state of holes. As the effect of an applied electric field is equivalent to the change in the effective confinement, the electric dependence of the hole g factor can be understood in the similar way [110].

For effective tuning of exciton g factors in single quantum dots a relatively strong electric field is usually required. It has already been shown that, with the same applied electric field, a double dot often exhibit a larger Stark shift compared with the single dot of the same dimension. The model system adopted here involves two coupled disk-like InAs quantum dots, each having a diameter of 15.3 nm, separated by a GaAs barrier with a thickness of 4.5 nm. Figure 13 plots the g factors of the ground and first excited hole states calculated as a function of the electric field for the coupled dots with a separation of $d = 4.5$ nm. A resonance structure can be seen in the spectra of hole g factors, which is very different from the monotonic dependence of their counterparts in the single quantum dots. The probability density of the ground and first hole excited states at $F = 0, 10$ kV/cm (off resonance) and $F = 5.4$ kV/cm (on resonance) is plotted to highlight the origin of the g factor

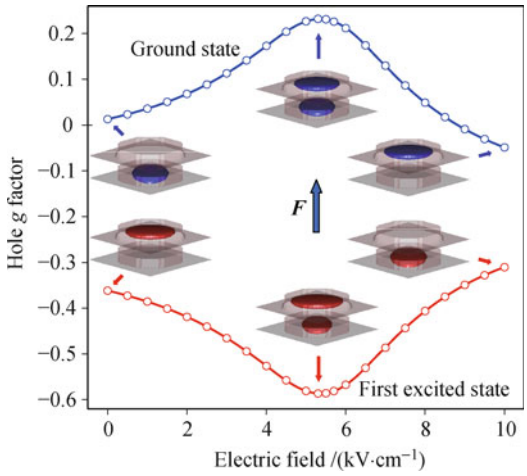

Fig. 13 g factors of the ground and first excited hole states in a lens-shaped double InAs/GaAs quantum dot, calculated as a function of the applied electric field. Probability density of the states at the various electric fields are illustrated. Reproduced from Ref. [111], Copyright © 2009 Institute of Physics.

resonances [111]. It is noted that recent theoretical work [112] by using the eight-band $\boldsymbol{k} \cdot \boldsymbol{p}$ method reports on the exciton g factors of the opposite sign to our result and the experiment [109]. Finally, we would like to point out that a magnetic impurity may lead to dramatic variation in electron g factors [113] though electrical tuning has been shown to be nearly ineffective.

2.6 Single InAs/InP self-assembled quantum dots on nanotemplates

Formation of self-assembled quantum dots during the Stranski–Krastanow growth of epitaxial layers is a very useful way of controlling matter in three dimensions in the one-dimensional growth. The disadvantage of this approach is the random in-plane nucleation of quantum dots and the variation of their sizes. Williams and coworkers [34, 115] proposed a different approach, involving growth of single InAs quantum dots on InP nanotemplates. The fabrication of nanotemplates starts with lithographically defined patterns for the initialization of the growth of InP pyramid. The starting area of the pyramid is defined with the accuracy of tens of nanometers. The growth of the pyramid is governed by the stability of crystallographic facets and, when interrupted, results in a formation of nanotemplates defined with atomic precision. InAs dots are grown on such nanotemplates and are covered with InP to complete the pyramid. Such structure, shown in Fig. 14(a), can be functionalized by either metallic gates or by building photonic crystals around them for a fully controlled light-matter system [36]. The first steps toward the theory of InAs quantum dots on InP templates have been made by some of us in Ref. [42].

As an example of a deterministically functionalized single quantum dot we show the result of the application of gates to the single quantum dot, resulting in a fully tunable optical structure. Figure 14(b) shows the emission spectrum of a single photo-excited quantum dot as a function of the bottom gate voltage. We see a number of emission lines, which correspond to charged exciton complexes X^0, X^-, X^{2-}, or different number of electrons N in the initial states (right-hand axis). The black circles and lines create a phase diagram of the emission spectrum as predicted in Ref. [27]. The emission for X^{2-} consists of two lines, corresponding to the singlet and triplet two-electron complexes in the final state, respectively. Hence, the electron spin can be detected optically. The effect of spin can also be seen in the emission from other multiexciton complexes.

Because the nanotemplate can be elongated, it allows for the control of the shape of the quantum dot. One would expect that the resulting splitting of the two p-shell states would be a measure of the elongation. Unfortunately this is not so straightforward. Figure 15(a) shows the InAs quantum dot on an elongated

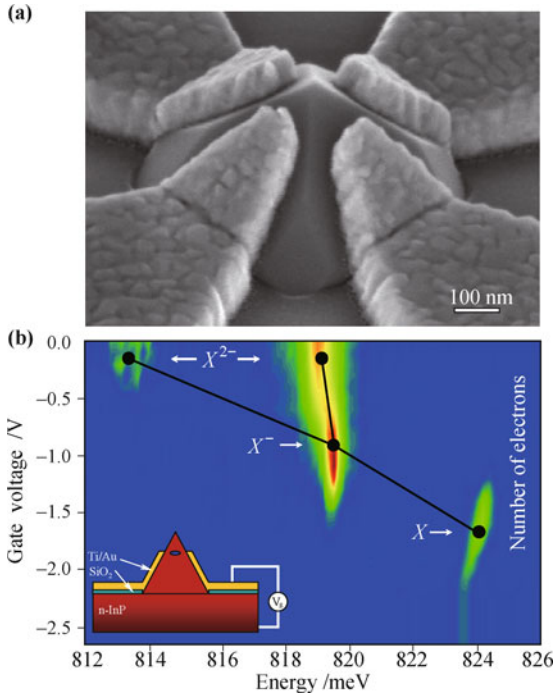

Fig. 14 **(a)** Single InAs quantum dot in an InP pyramid with metallic gates on the sides of the pyramid. **(b)** Emission spectrum as a function of the bottom gate voltage. Different emission lines correspond to different charged exciton states, X^0, X^-, X^{2-}, or different number of electrons in the initial states (right-hand axis). The black circles and lines create a phase diagram of the emission spectrum as predicted in Ref. [27]. Reproduced from Ref. [116], Copyright © 2009 Institute of Physics.

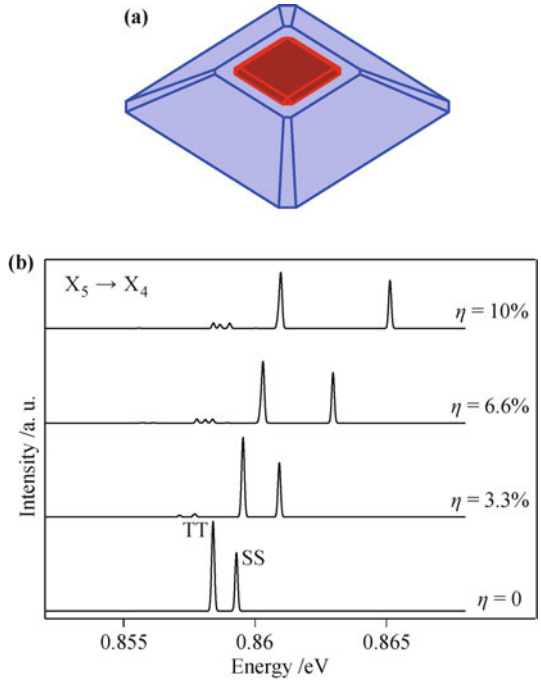

Fig. 15 **(a)** Schematic view of a single InAs quantum dot on a InP pyramid template. **(b)** Emission spectrum from the five-exciton to the four-exciton complex as a function of the elongation of the template. The two emission peaks correspond to two four-exciton final states, determined by spin for symmetric structure and splitting of the p shell for asymmetric structure. Reproduced from Ref. [42], Copyright © 2005 American Physical Society.

template. Figure 15(b) shows the emission from the five-exciton complex in which three electrons and three holes populate the two p-shell states. We see that even for a fully symmetric quantum dot there are two emission peaks. These two peaks correspond to two different four-exciton final states, singlet–singlet and triplet–triplet, which differ by exchange and correlation energy. As the structure becomes highly asymmetric, we can attempt to extract the p-shell splitting from the emission spectra. Much work is needed for the full understanding of InAs/InP quantum dots on patterned substrates to realize this promising technology.

3 Graphene quantum dots

3.1 Introduction

Carbon atom, a basis of organic chemistry, gives rise to a rich variety of chemical structures, allotropes, due to the flexibility of its π-bonds. One of the allotropes is graphene, a two-dimensional sheet of carbon atoms arranged in a hexagonal honeycomb lattice. The theory of graphene has been developed at the National Research Council of Canada by Wallace as early as 1947 [117]. Since then graphene was considered as a starting point in the understanding of other allotropes such as graphite (stack of graphene layers), carbon nanotubes (rolled-up cylinders of graphene), and fullerenes (wrapped graphene by the introduction of pentagones on the honeycomb lattice). Graphene has been investigated extensively in Graphite Intercalation Compounds (GIC) [118]. Intercalation of graphite with, e.g., Lithium or Potassium leads to increased separation of graphene sheets and introduction of electrons or holes. GIC were equivalent to doped semiconductors. The theory of optical properties of graphene in GIC was developed by Blinowski and co-workers [119] and by one of us [120] and has been compared with reflectivity experiments. The theory of electronic screening and plasmons in GIC was also developed at that time [121]. Recently, following the first experimental isolation of a single graphene sheet in 2004 by Geim, Novoselov and co-workers [37], both experimental and theoretical research on graphene has increased exponentially due to the unique physical properties and promising potential for applications [122].

One of the most interesting electronic properties of graphene is the zero-energy gap and relativistic nature of quasi-particle dispersion close to the Fermi level predicted by Wallace [117]: low energy excitations are massless Dirac fermions, mimicking the physics of quantum electrodynamics at much lower velocities than light. On the other hand, with ongoing improvements in nanofabrication techniques [123], the zero-energy gap of the Dirac quasi-particles can be opened by engineering the size,

shape, edge, and carrier density. This in turn offers possibilities to control electronic [38, 124–128, 130–132], magnetic [39, 123, 130–138] and optical [138–142] properties of a single-material nanostructure simultaneously. As a result, there is a growing interest in studying lower-dimensional structures such as graphene ribbons [144–147], and more recently graphene quantum dots [126–129, 130]. In the following we will concentrate on the electronic structure, optical properties and magnetism of graphene quantum dots. For transport properties, please refer to Ref. [143] for more detail review.

3.2 Electronic structure — Tight-binding approach

The sp^2 hybridization of carbon atom $2s$ and p_x, p_y orbitals leads to trigonal σ-bonds responsible for a robust hexagonal lattice of carbon atoms. The remaining p_z orbitals from each carbon atom form the π-band, which is well separated from the filled σ-band. Hence, the electronic states of graphene in the vicinity of the Fermi level can be understood in terms of p_z electrons on a hexagonal lattice. The hexagonal honeycomb lattice consists of two triangular sublattices as shown in Fig. 16. Red atoms form the sublattice A, and blue atoms form the sublattice B. There are two carbon atoms, of type A and B, in a unit cell. Following Wallace [117], the wavefunction of graphene can be written as a linear combination of p_z orbitals localized on sublattices A and B:

$$\Psi_k(\boldsymbol{r}) = \sum_{\boldsymbol{R}_A} A(\boldsymbol{R}_A)\phi_z(\boldsymbol{r}-\boldsymbol{R}_A) + \sum_{\boldsymbol{R}_B} B(\boldsymbol{R}_B)\phi_z(\boldsymbol{r}-\boldsymbol{R}_B) \tag{36}$$

where ϕ_z is a localized p_z orbital. $\boldsymbol{R}_\mu$ represents the position of an atom on sublattice $\mu = A$ or B, and is a function of the lattice vectors $\boldsymbol{a}_1$,$\boldsymbol{a}_2$, and $\boldsymbol{b}$ shown in Fig. 16. Within the tight-binding formalism, the Hamiltonian can be written as:

$$H = -\sum_{i,j,\sigma} t_{ij} c^\dagger_{i\sigma} c_{j\sigma} \tag{37}$$

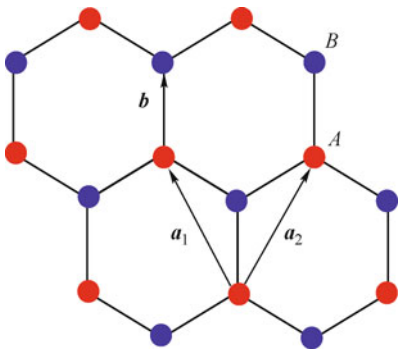

Fig. 16 Honeycomb lattice structure of graphene. The two interpenetrating triangular sublattices are illustrated by blue and red carbon atoms.

where the electrons can hop between sites i and j via the tunneling matrix element $t_{i,j}$. For graphene, the nearest neighbor hopping energy is about $t \approx 2.8$ eV and the next-nearest neighbor hopping energy $t' \approx 0.1$ eV [122]. For simplicity, let us consider only the first nearest neighbor interaction.

For bulk graphene the wave function that satisfies the periodicity of both sublattices can be classified by the wave vector k and written as:

$$\Psi_k(\boldsymbol{r}) = A_k \sum_{\boldsymbol{R}_A} \mathrm{e}^{\mathrm{i}\boldsymbol{k}\cdot\boldsymbol{R}_A}\phi_z(\boldsymbol{r}-\boldsymbol{R}_A) + B_k \sum_{\boldsymbol{R}_B} \mathrm{e}^{\mathrm{i}\boldsymbol{k}\cdot\boldsymbol{R}_{B+b}}\phi_z(\boldsymbol{r}-\boldsymbol{R}_B) \tag{38}$$

Solving the Schrödinger equation for graphene involves finding the solution for the coefficients of the two sublattices for each wave vector k:

$$\begin{pmatrix} 0 & tf(\boldsymbol{k}) \\ tf^*(\boldsymbol{k}) & 0 \end{pmatrix} \begin{pmatrix} A_k \\ B_k \end{pmatrix} = E \begin{pmatrix} A_k \\ B_k \end{pmatrix} \tag{39}$$

where

$$f(\boldsymbol{k}) = 1 + \mathrm{e}^{\mathrm{i}\boldsymbol{k}\cdot\boldsymbol{a}_1} + \mathrm{e}^{\mathrm{i}\boldsymbol{k}\cdot\boldsymbol{a}_2} \tag{40}$$

The energy spectrum E_k and the wave function are then given by

$$E(\boldsymbol{k}) = \pm t|f(\boldsymbol{k})| \tag{41}$$

$$A_k = \pm \mathrm{e}^{\mathrm{i}\theta_k} B_k \tag{42}$$

with θ_k being the phase of $f(\boldsymbol{k})$. The energy spectrum $E(\boldsymbol{k})$ is shown in Fig. 17. For the charge neutral system, each carbon atom gives one electron to the p_z orbital. As a result, the Fermi level is at $E(\boldsymbol{k}) = 0$, and the $\pm$ sign corresponds to the electron and hole branches, respectively. Although the electron-hole symmetry is conserved here, if one includes second neighbor interaction t', the electron and hole branches become asymmetric.

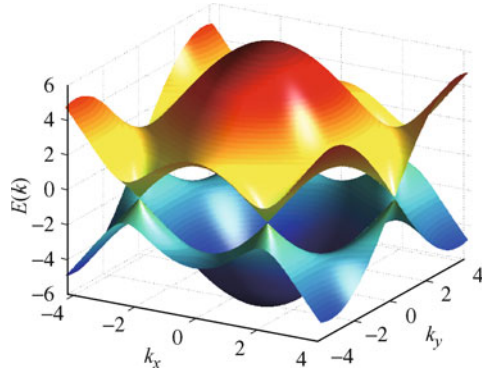

Fig. 17 Energy spectrum of graphene obtained from the nearest-neighbor tight-binding model.

3.3 Dirac fermions

One of the most striking properties of graphene is re-

vealed if we expand the energy spectrum close to Fermi level $E_{\mathbf{k}} = 0$, around the K and K' points of the Brillouin zone. In contrast with semiconductor quantum dots, where the energy spectrum $E(\boldsymbol{q}) = q^2/(2m)$ is quadratic, in graphene we find a linear dispersion

$$E(\boldsymbol{q}) \approx \pm v_{\mathrm{F}} q \tag{43}$$

where $\boldsymbol{q}$ is the momentum relative to one of the K or K' points, called Dirac points, and $v_{\mathrm{F}} = 3tb/2 \approx 10^6$ m/s is the velocity of Dirac fermions. We thus obtain relativistic-like dispersion relation with a velocity 300 times smaller than that of light. We can also expand Eq. (39) around one of the K points which gives the two-dimensional Dirac equation:

$$-\mathrm{i}v_{\mathrm{F}}\sigma \cdot \nabla\psi(\boldsymbol{r}) \approx E\psi(\boldsymbol{r}) \tag{44}$$

The wave functions around K and K' points are given by

$$\psi_{\pm}(\boldsymbol{k}) \approx \frac{1}{\sqrt{2}} \begin{pmatrix} \mathrm{e}^{-\mathrm{i}\theta_k} \\ \pm 1 \end{pmatrix} \text{ around } K \tag{45}$$

$$\frac{1}{\sqrt{2}} \begin{pmatrix} \mathrm{e}^{+\mathrm{i}\theta_k} \\ \pm 1 \end{pmatrix} \text{ around } K' \tag{46}$$

As discussed above, the wave function for Dirac Fermions has two components corresponding to the two sublattices. The two-component character is often referred to as pseudo-spin. In analogy with real spin, the Dirac Fermion wave function acquires Berry's phase if we adiabatically change the wave vector k along a closed loop enclosing the Dirac point. Hence the sublattice structure adds a nontrivial topological effect to the physics of graphene.

3.4 Graphene quantum dots

As we can see from Eq. (43) and Fig. 17, graphene is a gapless material. As a result, in analogy with the phenomenon of Klein tunneling for massless particles in relativistic quantum mechanics, it is not possible to confine Dirac electrons in graphene electrostatically using metallic gates as in semiconductor quantum dots. Various indirect ways were proposed for opening a gap to confine the electrons, such as size quantization in a graphene ribbon [144–147] or using bilayer graphene [148–155]. In this review we will focus on graphene islands with size quantization in the two dimensions, i.e., graphene quantum dots with edges created by, e.g., etching [123]. Quantum confinement in such systems was experimentally observed [38, 124, 125] and there is increasing interest in creating quantum dots with well controlled shapes and edges [123, 129].

3.5 Shape and edge effects

Graphene sheet can be cut along different crystallographic directions as seen in the top panel of Fig. 18, resulting in different types of edges. The most stable edge types are armchair and zigzag edges [156, 157]. Together with the shape of the quantum dot, the edge type plays an important role in determining the electronic, magnetic, and optical properties. In this section, we will compare the properties of quantum dots of various shape and edge, and study their properties as a function of their size. We consider three different quantum dots as illustrated in Fig. 18: (a) hexagonal dot with armchair edges, (b) hexagonal dot with zigzag edges, and (c) triangular dot with zigzag edges. Their energy spectra, shown on the lower panel of Fig. 18, were calculated by numerically solving the tight-binding Hamiltonian of Eq. (37) in the nearest neighbors approximation. Clearly the energy spectrum around the Fermi level ($E = 0$) strongly depends on the structure. While the hexagonal armchair and trigonal zigzag dots have a well defined gap of the order of $0.2t$ (shown by a red arrow), for the hexagonal zigzag dot the gap is much smaller. Moreover, in addition to valence and conduction bands, the trigonal zigzag dot spectrum shows a shell of degenerate levels at the Fermi level [39, 130, 132–136, 138]. As we will see in the following section, this degenerate band is responsible for interesting electronic and magnetic properties.

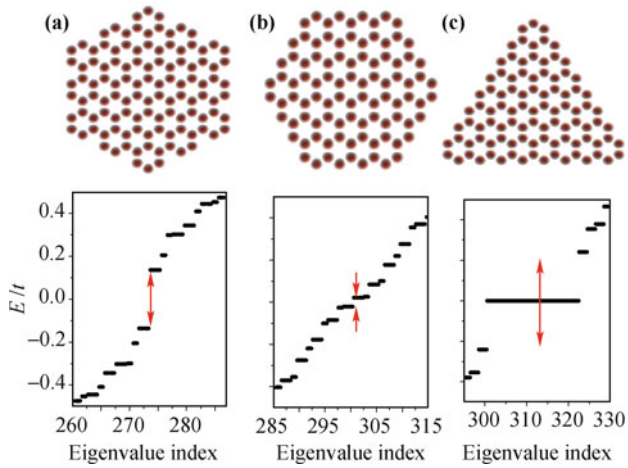

Fig. 18 Single-particle tight-binding spectrum of **(a)** armchair hexagonal, **(b)** zigzag hexagonal, and **(c)** zigzag triangular graphene quantum dot structures consisting of similar number of carbon atoms. Top panel shows the atomic positions. Reproduced from Ref. [133], Copyright © 2010 American Physical Society.

In order to understand further the electronic properties near the Fermi level, in Fig. 19 we plot the energy gap as a function of the number of atoms. For the hexagonal armchair dot (red dots), the gap decays as the inverse of the square root of number of atoms N, from hundred atom to million atom nanostructures. This is expected for confined Dirac fermions with photon-like linear energy dispersion ($E_{\mathrm{gap}} \propto k_{\mathrm{min}} \approx 2\pi/\Delta x \propto 1/\sqrt{N}$), as pointed out in Refs. [130, 139, 158]. However, the replacement of the edge from armchair to the zigzag has

a significant effect on the energy gap. The energy gap of hexagonal structure with zigzag edges decreases rapidly as the number of atoms increases. This is due to the zigzag edges leading to localized states at the edge of the quantum dot, similar to whispering gallery modes of photons localized at the edge of photonic microdisk [159]. Figure 19 also shows the effect on the energy gap of deforming the hexagonal structure into a triangle while keeping zigzag edges. Unlike the hexagonal zigzag structure, all three edges of the triangle are composed of atoms of the same sublattice. As a result, they do not hybridize and form a degenerate band at Fermi level. The energy gap shown in Fig. 19 corresponds to transitions from the topmost valence to the lowest conduction band state. The energy gap in the triangular zigzag structure follows the power law $E_{\rm gap} \propto \sqrt{N}$ since it is due to confinement of bulk states, whereas the gap for the hexagonal armchair structure is due to the hybridization of the edge states. We note that the energy gap changes from ≈ 2.5 eV (green light) for a quantum dot with ≈ 100 atoms to ≈ 30 meV (8 THz) for a quantum dot with a million atoms and a diameter of ~ 0.4 micrometer. The presence of a partially occupied band of degenerate states in the middle of a well defined energy gap offers unique opportunity to control magnetic and optical properties of triangular graphene nanostructures simultaneously.

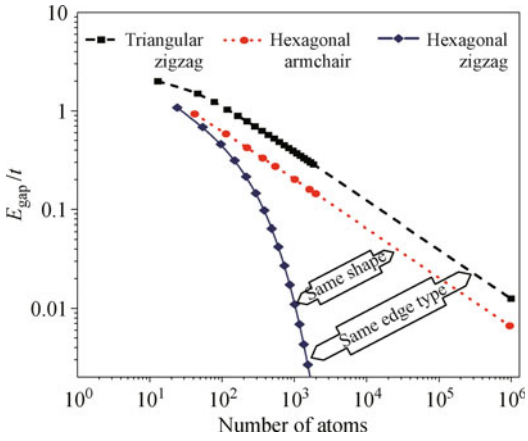

Fig. 19 Energy band gap as a function of number of carbon atoms for triangular zigzag, hexagonal armchair and hexagonal zigzag structures. Reproduced from Ref. [133], Copyright © 2010 American Physical Society.

3.6 Gated quantum dots: Beyond tight-binding approach

While the basic tight-binding model of Eq. (37) accurately describes the electronic properties of bulk graphene, the situation can be more complicated for gated finite-size systems. The experimental values used for first and second nearest neighbors hopping terms t and t' are based on the assumption that electronic occupation on every site is constant (equal to one), which may not be true at the edges of a quantum dot. Moreover, for a gated system, the average occupation per site can be higher or lower than one. Thus, one must take into account the deviation of the electronic density from the bulk values due to edge effects and doping via the electrostatic gate [39].

Interaction effects due to additional charge density on each site can be investigated within a mean-field approach using a combination of tight-binding and self-consistent Hartree–Fock methods (TB–HF). For p_z electrons, the interacting many-body Hamiltonian can be written as

$$H = -\sum_{il\sigma} t_{il\sigma} c^{\dagger}_{i\sigma} c_{l\sigma} + \frac{1}{2}\sum_{ijkl\sigma\sigma'} \langle ij|V|kl\rangle c^{\dagger}_{i\sigma} c^{\dagger}_{j\sigma'} c_{k\sigma'} c_{l\sigma} \quad (47)$$

and the corresponding mean-field Hartree–Fock Hamiltonian is

$$H_{\rm MF} = -\sum_{il\sigma} t_{il\sigma} c^{\dagger}_{i\sigma} c_{l\sigma} + \sum_{il\sigma}\sum_{jk\sigma'} \rho_{jk\sigma'}(\langle ij|V|kl\rangle - \langle ij|V|lk\rangle\delta_{\sigma\sigma'}) c^{\dagger}_{i\sigma} c_{l\sigma} \quad (48)$$

where the operator $c^{\dagger}_{i\sigma}$ creates a p_z electron on site i with spin σ. Note that at this stage the unknown hopping terms $t_{il\sigma}$ do not include the effect of electron–electron interactions. We want to express the Hamiltonian for our system as a function of experimentally measured bulk tight-binding parameters $\tau_{il\sigma}$. For the graphene sheet, the mean-field Hamiltonian is written as

$$H^{\rm bulk}_{\rm MF} = -\sum_{il\sigma} t_{il\sigma} c^{\dagger}_{i\sigma} c_{l\sigma} + \sum_{il\sigma}\sum_{jk\sigma'} \rho^{\rm bulk}_{jk\sigma'}(\langle ij|V|kl\rangle - \langle ij|V|lk\rangle\delta_{\sigma\sigma'}) c^{\dagger}_{i\sigma} c_{l\sigma} \quad (49)$$

$$\equiv -\sum_{il\sigma} \tau_{il\sigma} c^{\dagger}_{i\sigma} c_{l\sigma} \quad (50)$$

We can now re-express our mean-field Hamiltonian as

$$H_{\rm MF} = H_{\rm MF} - H^{\rm bulk}_{\rm MF} + H^{\rm bulk}_{\rm MF} = -\sum_{il\sigma} \tau_{il\sigma} c^{\dagger}_{i\sigma} c_{l\sigma} + \sum_{il\sigma}\sum_{jk\sigma'} (\rho_{jk\sigma'} - \rho^{\rm bulk}_{jk\sigma'})(\langle ij|V|kl\rangle - \langle ij|V|lk\rangle\delta_{\sigma\sigma'}) c^{\dagger}_{i\sigma} c_{l\sigma} \quad (51)$$

which must be solved self-consistently to obtain Hartree-Fock quasi-particle states.

In order to take into account the effect of induced gate charge away from charge neutrality, we assume that electrons in the graphene island interact with the electrons transferred to the gate via the term v^g_{ii} given by

$$v^g_{ii}(q_{\rm ind}) = \sum_{j=1}^{N_{\rm site}} \frac{-q_{\rm ind}/N_{\rm site}}{\kappa\sqrt{(x_i - x_j)^2 + (y_i - y_j)^2 + d^2_{\rm gate}}} \quad (52)$$

where (x_i, y_i) are the coordinates of the atoms. This model assumes that the induced charge $q_{\rm ind} = -\Delta N$ is smeared out at positions (x_i, y_i) at a distance $d_{\rm gate}$ from the quantum dot. Our final Hartree–Fock Hamiltonian is then given by

$$\begin{aligned} H_{\rm MF} = &-\sum_{il\sigma} \tau_{il\sigma} c^\dagger_{i\sigma} c_{l\sigma} \\ &+\sum_{il\sigma}\sum_{jk\sigma'} (\rho_{jk\sigma'} - \rho^{\rm bulk}_{jk\sigma'})(\langle ij|V|kl\rangle \\ &-\langle ij|V|lk\rangle\delta_{\sigma\sigma'}) c^\dagger_{i\sigma} c_{l\sigma} + \sum_{i\sigma} v^g_{ii}(q_{\rm ind}) c^\dagger_{i\sigma} c_{i\sigma} \quad (53) \end{aligned}$$

After self-consistent diagonalization of the Hamiltonian as in Eq. (53) for a TB–HF reference level defined by $N = N_{ref}$, we obtain TB+HF quasi-particles denoted by the creation operator $b^\dagger_p$, with eigenvalues ϵ_p and eigenfunctions $|p\rangle$. We can then start filling the conduction states above Fermi level one by one to investigate correlation effects. The general Hamiltonian for the whole system can be written as

$$H = H + H_{\rm MF} - H_{\rm MF}$$

from which, after extensive algebra, it can be shown that in the rotated basis of $b^\dagger_p$ quasi-particles and by neglecting scatterings from/to the degenerate shell, the Hamiltonian for $N_{\rm add} + N_{\rm ref}$ electrons reduces to the configuration interaction problem for the $N_{\rm add}$ added electrons given by

$$\begin{aligned} H = &\sum_{p\sigma} \epsilon_p b^\dagger_{p\sigma} b_{p\sigma} + \frac{1}{2}\sum_{pqrs\sigma\sigma'} \langle pq|V|rs\rangle b^\dagger_{p\sigma} b^\dagger_{q\sigma'} b_{r\sigma'} b_{s\sigma} \\ &+\sum_{pq\sigma} \langle p|v^g(N_{\rm add})|q\rangle b^\dagger_{p\sigma} b_{q\sigma} \\ &+2\sum_{p'} \langle p'|v^g(N_{\rm add})|p'\rangle \quad (54) \end{aligned}$$

where the indices without the prime sign (p, q, r, s) run over states above the TB–HF reference level, while the index with the prime sign p' runs over valence states (below the TB–HF reference level). Here the first term on the right-hand side represents the energies of quasiparticles; the second term describes the interaction between the added quasiparticles, the third term describes the interaction between the quasiparticles and the gate; and the last term is a constant giving the interaction energy between the $N_{\rm ref}$ electrons and the charge on the gate. We then build all possible many-body configurations within the degenerate shell for a given electron number $N_{\rm add}$, for which Hamiltonian matrices corresponding to different S_z subspaces are constructed and diagonalized.

3.7 Magnetism in triangular quantum dots

As discussed in the previous section, when an electron is confined to a triangular atomic thick layer of graphene with zigzag edges, its energy spectrum collapses to a shell of degenerate states at the Fermi level (the Dirac point). This is similar to the edge states in graphene ribbons [144–147], but the shell is isolated from the other states by a gap. Indeed, the zigzag edge breaks the symmetry between the two sublattices of the honeycomb lattice, behaving like a defect. Therefore, electronic states localized on the zigzag edges appear with energy in the vicinity of the Fermi level. The degeneracy $N_{\rm edge}$ is proportional to the edge size and can be made macroscopic. A non-trivial question addressed here is the specific spin and orbital configuration of the electrons as a function of the size and the fractional filling of the degenerate shell of edge states. Due to the strong degeneracy, many-body effects can be expected to be as important as in the fractional quantum Hall effect, but without the need for a magnetic field. Calculations based on the Hubbard approximation [134, 135] and local spin density functional theory [135, 136] showed that the neutral system (i.e., at half-filling) has its edge states polarized.

In order to study many-body effects within the charged degenerate shell using the configuration interaction method, we first perform a Hartree–Fock calculation for the charged system of $N - N_{\rm edge}$ electrons, with empty degenerate shell and $N_{\rm edge}$ electrons transferred to the gate, as shown in Fig. 20 (a). The spectrum of HF quasi-particles is shown in Fig. 20 (b) with black lines. Due to the mean-field interaction with the valence electrons and charged gate, a group of three states is now separated from the rest by a small gap of ~ 0.2 eV. The three states correspond to HF quasiparticles localized in the three corners of the triangle. The same physics occurs in density functional calculation within local density approximation (LDA), shown in the inset of Fig. 20 (b). Hence we see that the shell of almost degenerate states with a well defined gap separating them from the valence and conduction bands exists in the three approaches.

The wave functions corresponding to the shell of nearly-degenerate zero-energy states obtained from TB-HF calculations are used as a basis set in our configuration interaction calculations where we add $N_{\rm add}$ electrons from the gate to the shell of degenerate states. In Fig. 21, total spin S of the ground state as a function of the filling of the degenerate shell is shown for different sizes of quantum dots. Three aspects of these results are particularly interesting: (i) for the charge neutral case ($N_{\rm add} - N_{\rm edge} = 0$), for all the island sizes studied ($N_{\rm edge} = 3 - 7$), the half-filled shell is maximally spin polarized as indicated by red arrows, in agreement with DFT calculations [135, 136]. The polarization of the half-filled shell is also consistent with the Lieb theorem for the Hubbard model for bipartite lattice [160]. (ii) The spin polarization is fragile away from half-filling. If we add one extra electron ($N_{\rm add} - N_{\rm edge} = 1$), magnetization

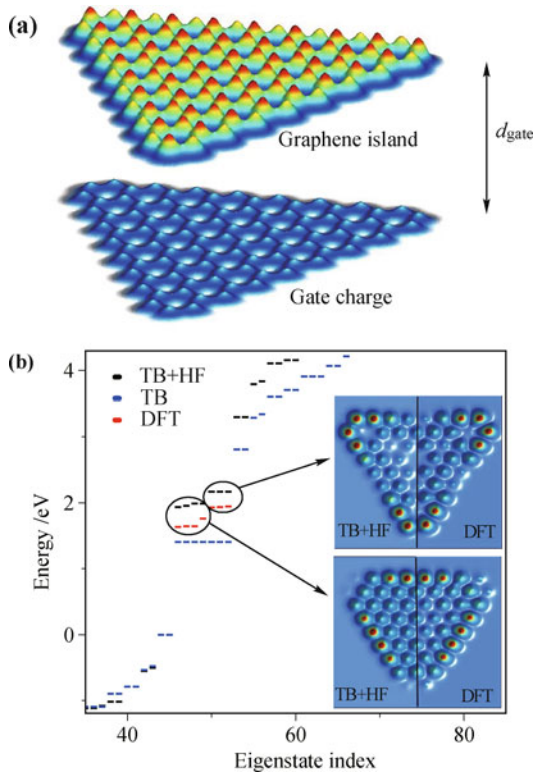

Fig. 20 **(a)** Electronic density in a triangular graphene island of 97 carbon atoms where 7 electrons were moved to the metallic gate at a distance of d_{gate}. **(b)** Single particle spectrum of the structure in (a), obtained by tight-binding (TB, blue lines) and self-consistent Hartree–Fock (TB+HF, black lines) methods. The 7 zero-energy states near the Fermi level are compared to DFT results. In Hartree–Fock and DFT calculations 7 electrons were removed, leaving the zero-energy states empty. The dielectric constant κ is set to 6. Inset compares the structure of corner and side states obtained using Hartree–Fock and DFT calculations. In DFT calculations, hydrogen atoms were attached to dangling bonds. Reproduced from Ref. [39], Copyright © 2009 American Physical Society.

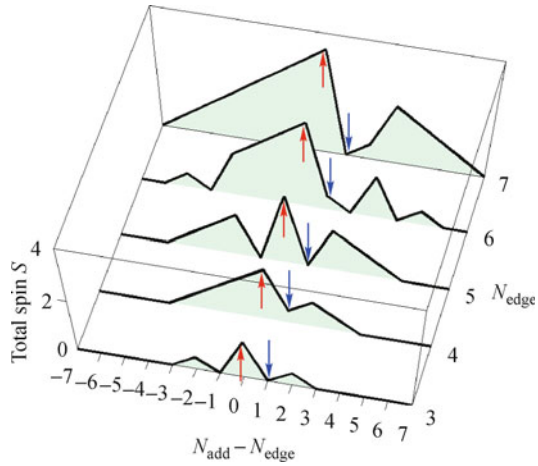

Fig. 21 Spin phase diagram from configuration interaction calculations for different sizes of the triangular dot characterized by the number of edge states N_{edge}, as a function of the filling of the zero-energy states $N_{add} - N_{edge}$. Charge neutral case corresponds to $N_{add} - N_{edge} = 0$, for which the total spin of the zero-energy electrons are always maximized ($S = N_{edge}/2$, indicated by red arrows). If the quantum dot is charged by 1 electron ($N_{add} - N_{edge} = 1$) then the total spin has minimum value, i.e. $S = 0$ if N_{add} is even, $S = 1/2$ if N_{add} is odd (indicated by blue arrows). Reproduced from Ref. [39], Copyright © 2009 American Physical Society.

of the island collapses to the minimum possible value, as indicated by blue arrows in Fig. 21. Full or partial depolarization occurs for other filling numbers. (iii) The spin phase diagram is not necessarily symmetric around $N_{add} - N_{edge} = 0$. This is due to the imbalance between the two types of atoms of the honeycomb lattice in the triangular zig–zag structure, and the next nearest neighbor hopping term that breaks the electron–hole symmetry. Also, the spin depolarization at half-filling was found to be insensitive to the screening of electron–electron interactions, as values of dielectric screening constant κ between 2 and 8 led to the same behavior of the charge-neutral and single electron charged cases (which is not shown).

3.8 Excitons in triangular quantum dots

The degenerate band of zero-energy states in triangular dots discussed in the previous section leads to unusual optical properties. Indeed, we can classify allowed optical transitions into four classes: (i) from doubly occupied valence states to zero-energy degenerate band, (ii) from zero-energy band to empty conduction band, (iii) from valence band to conduction band, and finally (iv) within zero-energy states. As a consequence, there are three different photon energy scales involved in the absorption spectrum, with their properties depending on the size and the filling of the degenerate band. In this work we focus on excitonic effects at half-filling. A detailed analysis of excitonic transitions away from half-filling can be found in Ref. [133].

Figure 22(a) schematically illustrates the optical transition processes between the doubly-occupied valence band states towards the zero-energy band. As discussed earlier, at half-filling the zero-energy states are singly occupied with spin polarized electrons. Therefore an up-spin electron from the valence band can be excited to the zero-energy band through photon absorption, leaving behind a down-spin hole. Note that optical transitions that conserve the total spin within zero-energy band are not allowed. The possibility to allow transitions within zero-energy band by gate charging the system is discussed in Ref. [133]. Figure 22(b)–(d) illustrates in detail the effect of electron–electron and final-state (excitonic) interactions on the absorption spectra. Figure 22(b) shows the detailed VZ absorption spectrum for noninteracting electrons. This spectrum corresponds to transitions from the filled valence band to half-filled shell of zero-energy states. Half-filling implies that each

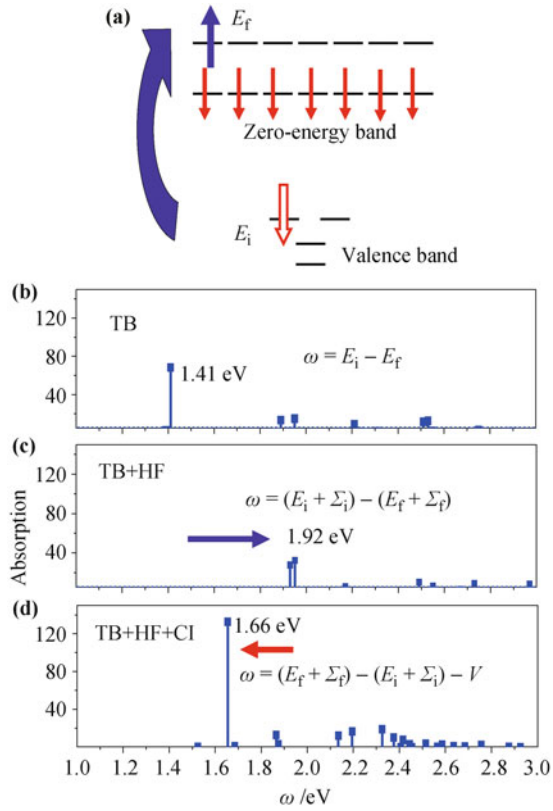

Fig. 22 **(a)** Single particle tight-binding energies of states near Fermi level for a N=97-atom triangular zigzag quantum dot. The colored arrows represent optical transitions from valence to conduction band (VC, green), valence to zero-energy band (VZ, blue), zero-energy to conduction band (ZC, red) and zero-energy to zero-energy band (ZZ, black). Figures **(b)**–**(d)** shows the effect of electron–electron interactions on the VZ transitions within (c) Hartree–Fock approximation, and including (d) correlations and excitonic effect obtained from exact configuration interaction calculations.

state of the zero-energy band is optically allowed. Numerical and analytical calculations show that among the zero-energy states there are two bulklike states, which couple strongly to the valence band resulting in the main transition at $E = 1.41$ eV. When the electron–electron interactions are turned on within Hartree–Fock level, the photon energies corresponding to optical transitions $\omega = (E_f + \Sigma_f) - (E_i + \Sigma_i)$ are renormalized by the difference in quasi-particle self-energies $\Sigma_f - \Sigma_i$. The absorption spectrum, shown in Fig. 22(c), is renormalized with transition energies blue-shifted by 0.51 eV to E= 1.92 eV. Finally, when final-state interactions between all interacting quasi-electron and quasi-hole states are taken into account, the excitonic spectrum is again renormalized from the quasi-particle spectrum, with transitions red shifted from quasi-particle transitions at E= 1.92 eV, down to $E = 1.66$ eV. As we can see, electron–electron interactions play an important role in determining energies and form of the absorption spectrum, with net blue shift from the noninteracting spectrum by 0.25 eV.

3.9 Effect of imperfections

Clearly, it is a challenging task to fabricate structures without imperfections, although there is considerable experimental effort for creating quantum dots with well controlled shapes and edges [123, 129]. Therefore an interesting question is the effect of various types of defects on the electronic properties. For triangular structures, the robustness of the zigzag edges to pentagon-heptagon reconstruction was established in Ref. [157]. If properly hydrogenated, zigzag edges were found to be more stable than the reconstructed ones. On the other hand, in a triangular zigzag dot with a missing corner, it was found that [132] the degenerate band of zero energy states survives. Finally, the magnetization of the edges described above is expected to be robust against defects, since Lieb's theorem [160] guarantees that magnetization as long as the biparticity of the honeycomb lattice is not distorted. To understand the effect of strong distortion of the biparticity or the honeycomb structure of the lattice, future work is necessary.

4 Conclusions

To summarize, we have reviewed here our recent work on the electronic and optical properties of semiconductor and graphene quantum dots. The quantum dots allow us to manipulate quantum states and design quantum systems at the many-particle level. New phenomena have been uncovered and described in this review, and it is hoped that many discoveries await us in the future.

Acknowledgements This work was supported by the National Natural Science Foundation of China (Grant No. 60876087), NRC-NSERC-BDC nanotechnology programs, Canadian Institute for Advanced Research, and NRC-CNRS Collaborative Research Project. M. Zieliński would like to acknowledge the support of the Foundation for Polish Science, Homing Plus Programme co-financed by the European Union within the European Regional Development Fund. Fruitful discussions with A. Sachrajda, G. Austing, S. Studenikin, R. Williams, D. Dalacu, P. Poole, S. Raymond of IMS, M. Potemski (Grenoble) and M. Bayer (Dortmund) are acknowledged.

References

1. L. Jacak, P. Hawrylak, and A. Wojs, Quantum Dots, Berlin: Springer, 1998
2. D. Bimberg, M. Grundmann, and N. N. Ledentsov, Quantum Dot Heterostructures, Chichester: Wiley, 1999
3. P. Hawrylak, and M. Korkusinski, Electronic Properties of Self-Assembled Quantum Dots, in: Single Quantum Dots — Fundamentals, Applications, and New Concepts, edited by P. Michler, Topics in Applied Physics, Berlin: Springer, 2003
4. M. Korkusinski and P. Hawrylak, Coded qubit based on electron spin, in: Semiconductor Quantum Bits, edited by O. Benson and F. Henneberger, Singapore: Pan Stanford Pub-

lishing, 2008

5. P. Hawrylak, Magnetic ion-carrier interactions in quantum dots, pp 191–220, in: Introduction to the Physics of Diluted Magnetic Semiconductors, edited by Jacek Kossut and Jan Gaj, Springer Series in Materials Science 144, 2011
6. B. Trauzettel, D. V. Bulaev, D. Loss, and G. Burkard, Nat. Phys., 2007, 3(3): 192
7. P. Hawrylak, Phys. Rev. Lett., 1993, 71(20): 3347
8. P. Hawrylak, C. Gould, A. Sachrajda, Y. Feng, and Z. Wasilewski, Phys. Rev. B, 1999, 59(4): 2801
9. M. Ciorga, A. S. Sachrajda, P. Hawrylak, C. Gould, P. Zawadzki, S. Jullian, Y. Feng, and Z. Wasilewski, Phys. Rev. B, 2000, 61(24): R16315
10. M. Bayer, P. Hawrylak, K. Hinzer, S. Fafard, M. Korkusinski, Z. R. Wasilewski, O. Stern, and A. Forchel, Science, 2001, 291(5503): 451
11. J. M. Elzerman, R. Hanson, J. S. Greidanus, L. H. Willems van Beveren, S. De Franceschi, L. M. K. Vandersypen, S. Tarucha, and L. P. Kouwenhoven, Phys. Rev. B, 2003, 67(16): 161308
12. J. R. Petta, A. C. Johnson, C. M. Marcus, M. P. Hanson, and A. C. Gossard, Phys. Rev. Lett., 2004, 93(18): 186802
13. M. Pioro-Ladrière, M. Ciorga, J. Lapointe, P. Zawadzki, M. Korkusinski, P. Hawrylak, and A. S. Sachrajda, Phys. Rev. Lett., 2003, 91(2): 026803
14. P. Hawrylak and M. Korkusiński, Solid State Commun., 2005, 136(9–10): 508
15. L. Gaudreau, S. A. Studenikin, A. S. Sachrajda, P. Zawadzki, A. Kam, J. Lapointe, M. Korkusinski, and P. Hawrylak, Phys. Rev. Lett., 2006, 97(3): 036807
16. M. Korkusinski, I. P. Gimenez, P. Hawrylak, L. Gaudreau, S. A. Studenikin, and A. S. Sachrajda, Phys. Rev. B, 2007, 75(11): 115301
17. G. Granger, L. Gaudreau, A. Kam, M. Pioro-Ladrière, S. A. Studenikin, Z. R. Wasilewski, P. Zawadzki, and A. S. Sachrajda, Phys. Rev. B, 2010, 82(7): 075304
18. L. Goldstein, F. Glas, J. Y. Marzin, M. N. Charasse, and G. Le Roux, Appl. Phys. Lett., 1985, 47(10): 1099
19. P. M. Petroff, Epitaxial Growth and Electronic Structure of Quantum Dots, in: Single Quantum Dots — Fundamentals, Applications, and New Concepts, edited by P. Michler, Topics in Applied Physics, Berlin: Springer, 2003
20. Y. Arakawa and H. Sakaki, Appl. Phys. Lett., 1982, 40(11): 939
21. N. N. Ledentsov, Semicond. Sci. Technol., 2011, 26(1): 014001
22. S. Fafard, K. Hinzer, S. Raymond, M. Dion, J. McCaffrey, Y. Feng, and S. Charbonneau, Science, 1996, 274(5291): 1350
23. M. V. Maximov, Yu. M. Shernyakov, A. F. Tsatsul'nikov, A. V. Lunev, A. V. Sakharov, V. M. Ustinov, A. Yu. Egorov, A. E. Zhukov, A. R. Kovsh, P. S. Kop'ev, L. V. Asryan, Zh. I. Alferov, N. N. Ledentsov, D. Bimberg, A. O. Kosogov, and P. Werner, J. Appl. Phys., 1998, 83(10): 5561
24. S. Fafard, Z. R. Wasilewski, C. Ni Allen, K. Hinzer, J. P. McCaffrey, and Y. Feng, Appl. Phys. Lett., 1999, 75(7): 986
25. G. Ortner, C. Ni Allen, C. Dion, P. Barrios, D. Poitras, D. Dalacu, G. Pakulski, J. Lapointe, P. J. Poole, W. Render, and S. Raymond, Appl. Phys. Lett., 2006, 88(12): 121119
26. C. E. Valdivia, E. Desfonds, D. Masson, S. Fafard, A. Carlson, J. Cook, T. J. Hall, and K. Hinzer, Proc. SPIE, 2008, 7099: 709915
27. A. Wojs and P. Hawrylak, Phys. Rev. B, 1997, 55(19): 13066
28. A. Wojs and P. Hawrylak, Solid State Commun., 1996, 100(7): 487
29. P. Hawrylak and A. Wojs, Semicond. Sci. Technol., 1996, 11(11S): 1516
30. P. Hawrylak, Phys. Rev. B, 1999, 60(8): 5597
31. M. Bayer, O. Stern, P. Hawrylak, S. Fafard, and A. Forchel, Nature, 2000, 405(6789): 923
32. P. Hawrylak, Solid State Commun., 2003, 127(12): 793
33. P. Hawrylak, G. A. Narvaez, M. Bayer, and A. Forchel, Phys. Rev. Lett., 2000, 85(2): 389
34. J. Lefebvre, P. J. Poole, J. Fraser, G. C. Aers, D. Chithrani, and R. L. Williams, J. Cryst. Growth, 2002, 234(2–3): 391
35. M. E. Reimer, M. Korkusinski, D. Dalacu, J. Lefebvre, J. Lapointe, P. J. Poole, G. C. Aers, W. R. McKinnon, P. Hawrylak, and R. L. Williams, Phys. Rev. B, 2008, 78(19): 195301
36. D. Dalacu, K. Mnaymneh, V. Sazonova, P. J. Poole, G. C. Aers, J. Lapointe, and R. Cheriton A. J. Spring Thorpe, and R.Williams, Phys. Rev. B, 2010, 82(3): 033301
37. K. S. Novoselov, A. K. Geim, S. V. Morozov, D. Jiang, Y. Zhang, S. V. Dubonos, I. V. Grigorieva, and A. A. Firsov, Science, 2004, 306(5696): 666
38. T. Ihn, S. Gustavsson, U. Gasser, B. Küng, T. Müller, R. Schleser, M. Sigrist, I. Shorubalko, R. Leturcq, and K. Ensslin, Solid State Commun., 2009, 149(35–36): 1419
39. A. D. Güçlü P. Potasz, O. Voznyy, M. Korkusinski, and P. Hawrylak, Phys. Rev. Lett., 2009, 103(24): 246805
40. O. Stier, M. Grundmann, and D. Bimberg, Phys. Rev. B, 1999, 59(8): 5688
41. C. Pryor, J. Kim, L. W. Wang, A. J. Williamson, and A. Zunger, J. Appl. Phys., 1998, 83(5): 2548
42. W. Sheng and P. Hawrylak, Phys. Rev. B, 2005, 72(3): 035326
43. G. L. Bir and G. E. Pikus, Symmetry and Strain-Induced Effects in Semiconductors, New York: Wiley, 1974
44. A. Zhou and W. Sheng, Eur. Phys. J. B, 2009, 68(2): 233
45. L. R. C. Fonseca, J. L. Jimenez, and J. P. Leburton, Phys. Rev. B, 1998, 58(15): 9955
46. A. Wojs, P. Hawrylak, S. Fafard, and L. Jacak, Phys. Rev. B, 1996, 54(8): 5604
47. Z. R. Wasilewski, S. Fafard, and J. P. McCaffrey, J. Cryst. Growth, 1999, 201–202: 1131
48. S. Raymond, S. Studenikin, A. Sachrajda, Z. Wasilewski, S. J. Cheng, W. Sheng, P. Hawrylak, A. Babinski, M. Potemski, G. Ortner, and M. Bayer, Phys. Rev. Lett., 2004, 92(18): 187402
49. S. L. Chuang, Physics of Optoelectronic Devices, New York: Wiley, 1995
50. T. B. Bahder, Phys. Rev. B, 1990, 41(17): 11992
51. J. K. Cullum and R. A. Willoughby, Lanczos Algorithms for Large Symmetric Eigenvalue Computations, Philadelphia: SIAM, 2002
52. W. Sheng and J.-P. Leburton, Phys. Stat. Sol. (b), 2003, 237: 394
53. W. Sheng and J.-P. Leburton, Phys. Rev. B, 2001, 63: 161301(R)
54. W. Sheng and J.-P. Leburton, Appl. Phys. Lett., 2002, 81(23): 4449

55. J. I. Climente, M. Korkusinski, G. Goldoni, and P. Hawrylak, Phys. Rev. B, 2008, 78(11): 115323
56. C. Y. Hsieh, R. Cheriton, M. Korkusinski, and P. Hawrylak, Phys. Rev. B, 2009, 80(23): 235320
57. M. F. Doty, J. I. Climente, M. Korkusinski, M. Scheibner, A. S. Bracker, P. Hawrylak, and D. Gammon, Phys. Rev. Lett., 2009, 102(4): 047401
58. Y. C. Chang, Phys. Rev. B, 1988, 37(14): 8215
59. J. P. Loehr, Phys. Rev. B, 1994, 50(8): 5429
60. S. J. Sun and Y. C. Chang, Phys. Rev. B, 2000, 62(20): 13631
61. M. Zieliński, M. Korkusinski, and P. Hawrylak, Phys. Rev. B, 2010, 81(8): 085301
62. E. S. Kadantsev, M. Zielinski, M. Korkusinski, and P. Hawrylak, J. Appl. Phys., 2010, 107(10): 104315
63. E. S. Kadantsev and P. Hawrylak, Appl. Phys. Lett., 2011, 98(2): 023108
64. L. He and A. Zunger, Phys. Rev. B, 2006, 73(11): 115324
65. A. J. Williamson, L. W. Wang, and A. Zunger, Phys. Rev. B, 2000, 62(19): 12963
66. A. Canning, L. W. Wang, A. Williamson, and A. Zunger, J. Comput. Phys., 2000, 160(1): 29
67. G. Bester and A. Zunger, Phys. Rev. B, 2005, 71(4): 045318
68. D. J. Chadi, Phys. Rev. B, 1977, 16(2): 790
69. J. C. Slater and G. F. Koster, Phys. Rev., 1954, 94(6): 1498
70. P. Vogl, H. P. Hjalamarson, and J. D. Dow, J. Phys. Chem. Solids, 1983, 44(5): 365
71. J. M. Jancu, R. Scholz, F. Beltram, and F. Bassani, Phys. Rev. B, 1998, 57(11): 6493
72. G. Klimeck, R. C. Bowen, T. B. Boykin, and T. A. Cwik, Superlattices Microstruct., 2000, 27(5–6): 519
73. T. B. Boykin, G. Klimeck, R. C. Bowen, and F. Oyafuso, Phys. Rev. B, 2002, 66(12): 125207
74. J. G. Díaz and G. W. Bryant, Phys. Rev. B, 2006, 73(7): 075329
75. S. Lee, F. Oyafuso, P. von Allmen, and G. Klimeck, Phys. Rev. B, 2004, 69(4): 045316
76. W. Sheng and J. P. Leburton, Appl. Phys. Lett., 2002, 80(15): 2755
77. Y. Nabetani, T. Ishikawa, S. Noda, and A. Sasaki, J. Appl. Phys., 1994, 76(1): 347
78. W. Sheng, Appl. Phys. Lett., 2006, 89(17): 173129
79. W. Sheng, Appl. Phys. Lett., 2008, 92(4): 043113
80. W. Sheng and S. J. Xu, Phys. Rev. B, 2008, 77(11): 113305
81. M. Bayer, G. Ortner, O. Stern, A. Kuther, A. A. Gorbunov, A. Forchel, P. Hawrylak, S. Fafard, K. Hinzer, T. L. Reinecke, S. N. Walck, J. P. Reithmaier, F. Klopf, and F. Schäfer, Phys. Rev. B, 2002, 65(19): 195315
82. O. Benson, C. Santori, M. Pelton, and Y. Yamamoto, Phys. Rev. Lett., 2000, 84(11): 2513
83. N. Akopian, N. H. Lindner, E. Poem, Y. Berlatzky, J. Avron, D. Gershoni, B. D. Gerardot, and P. M. Petroff, Phys. Rev. Lett., 2006, 96(13): 130501
84. W. Sheng, S. J. Cheng, and P. Hawrylak, Phys. Rev. B, 2005, 71(3): 035316
85. T. Kazimierczuk, M. Goryca, M. Koperski, A. Golnik, J. A. Gaj, M. Nawrocki, P. Wojnar, and P. Kossacki, Phys. Rev. B, 2010, 81(15): 155313
86. T. Takagahara, Phys. Rev. B, 1993, 47(8): 4569
87. T. Takagahara, Phys. Rev. B, 2000, 62(24): 16840
88. S. V. Gupalov and E. L. Ivchenko, Phys. Solid State, 2000, 42(11): 2030
89. E. Kadantsev and P. Hawrylak, Phys. Rev. B, 2010, 81(4): 045311
90. G. Bester, S. Nair, and A. Zunger, Phys. Rev. B, 2003, 67: 161306(R)
91. R. Seguin, A. Schliwa, S. Rodt, K. Pötschke, U. W. Pohl, and D. Bimberg, Phys. Rev. Lett., 2005, 95(25): 257402
92. A. J. Shields, Nat. Photon., 2007, 1(4): 215
93. K. Kowalik, O. Krebs, A. Golnik, J. Suffczynski, P. Wojnar, J. Kossut, J. A. Gaj, and P. Voisin, Phys. Rev. B, 2007, 75(19): 195340
94. S. J. Cheng, W. Sheng, and P. Hawrylak, Phys. Rev. B, 2003, 68(23): 235330
95. A. Babinski, M. Potemski, S. Raymond, J. Lapointe, and Z. R. Wasilewski, Phys. Rev. B, 2006, 74(15): 155301
96. M. Bayer, A. Kuther, A. Forchel, A. Gorbunov, V. B. Timofeev, F. Schäfer, J. P. Reithmaier, T. L. Reinecke, and S. N. Walck, Phys. Rev. Lett., 1999, 82(8): 1748
97. G. Medeiros-Ribeiroa, M. V. B. Pinheiro, V. L. Pimentel, and E. Marega, Appl. Phys. Lett., 2002, 80(22): 4229
98. T. P. M. Alegre, F. G. G. Hernández, A. L. C. Pereira, and G. Medeiros-Ribeiro, Phys. Rev. Lett., 2006, 97(23): 236402
99. W. Sheng, S. J. Xu, and P. Hawrylak, Phys. Rev. B, 2008, 77: 241307(R)
100. W. Sheng, Appl. Phys. Lett., 2009, 94(12): 123113
101. W. Sheng and A. Babinski, Phys. Rev. B, 2007, 75(3): 033316
102. W. Sheng and P. Hawrylak, Phys. Rev. B, 2006, 73(12): 125331
103. W. Sheng and J. Wang, Phys. Rev. B, 2010, 82(7): 073308
104. K. Chang and J. B. Xia, Solid State Commun., 1997, 104(6): 351
105. P. W. Fry, I. E. Itskevich, D. J. Mowbray, M. S. Skolnick, J. J. Finley, J. A. Barker, E. P. O'Reilly, L. R. Wilson, I. A. Larkin, P. A. Maksym, M. Hopkinson, M. Al-Khafaji, J. P. R. David, A. G. Cullis, G. Hill, and J. C. Clark, Phys. Rev. Lett., 2000, 84(4): 733
106. K. Kowalik, O. Krebs, A. Lemaître, S. Laurent, P. Senellart, P. Voisin, and J. A. Gaj, Appl. Phys. Lett., 2005, 86(4): 041907
107. M. M. Vogel, S. M. Ulrich, R. Hafenbrak, P. Michler, L. Wang, A. Rastelli, and O. G. Schmidt, Appl. Phys. Lett., 2007, 91(5): 051904
108. T. Nakaoka, S. Tarucha, and Y. Arakawa, Phys. Rev. B, 2007, 76(4): 041301R
109. M. F. Doty, M. Scheibner, I. V. Ponomarev, E. A. Stinaff, A. S. Bracker, V. L. Korenev, T. L. Reinecke, and D. Gammon, Phys. Rev. Lett., 2006, 97(19): 197202
110. W. Sheng, Appl. Phys. Lett., 2010, 96(13): 133102
111. W. Sheng, Appl. Phys. Lett., 2009, 95(11): 113105
112. T. Andlauer and P. Vogl, Phys. Rev. B, 2009, 79(4): 045307
113. K. Chang, J. B. Xia, and F. M. Peeters, Appl. Phys. Lett., 2003, 82(16): 2661
114. M. Korkusinski, M. E. Reimer, R. L. Williams, and P. Hawrylak, Phys. Rev. B, 2009, 79(3): 035309
115. R. L. Williams, G. C. Aers, J. Lefebvre, P. J. Poole, and D. Chithrani, Physica E, 2002, 13(2–4): 1200

116. M. E. Reimer, D. Dalacu, J. Lapointe, P. J. Poole, D. Kim, G. C. Aers, W. R. McKinnon, and R. L. Williams, Appl. Phys. Lett., 2009, 94(1): 011108
117. P. R. Wallace, Phys. Rev., 1947, 71(9): 622
118. M. S. Dresselhaus and G. Dresselhaus, Adv. Phys., 1981, 30(2): 139
119. J. Blinowski, N. H. Hau, C. Rigaux, J. P. Vieren, R. Le Toullec, G. Furdin, A. Hérold, and J. Melin, J. Physique, 1980, 41(1): 47
120. D. M. Hoffman, P. C. Eklund, R. E. Heinz, P. Hawrylak, and K. R. Subbaswamy, Phys. Rev. B, 1985, 31(6): 3973
121. P. Hawrylak, Solid State Commun., 1987, 63(3): 241
122. A. H. C. Neto, F. Guinea, N. M. R. Peres, K. S. Novoselov, and A. K. Geim, Rev. Mod. Phys., 2009, 81(1): 109
123. L. C. Campos, V. R. Manfrinato, J. D. Sanchez-Yamagishi, J. Kong, and P. Jarillo-Herrero, Nano Lett., 2009, 9(7): 2600
124. J. S. Bunch, Y. Yaish, M. Brink, K. Bolotin, and P. L. McEuen, Nano Lett., 2005, 5(2): 287
125. L. A. Ponomarenko, F. Schedin, M. I. Katsnelson, R. Yang, E. W. Hill, K. S. Novoselov, and A. K. Geim, Science, 2008, 320(5874): 356
126. B. Wunsch, T. Stauber, and F. Guinea, Phys. Rev. B, 2008, 77(3): 035316
127. J. Wurm, A. Rycerz, I. Adagideli, M. Wimmer, K. Richter, and H. U. Baranger, Phys. Rev. Lett., 2009, 102(5): 056806
128. F. Libisch, C. Stampfer, and J. Burgdorfer, Phys. Rev. B, 2009, 79(11): 115423
129. J. Lu, P. S. Yeo, C. K. Gan, P. Wu, and K. P. Loh, Nat. Nanotechnol., 2011, 6(4): 247
130. J. Akola, H. P. Heiskanen, and M. Manninen, Phys. Rev. B, 2008, 77(19): 193410
131. M. Ezawa, Phys. Rev. B, 2010, 81(20): 201402
132. P. Potasz, A. D. Güçlü and P. Hawrylak, Phys. Rev. B, 2010, 81(3): 033403
133. A. D. Güçlü P. Potasz, and P. Hawrylak, Phys. Rev. B, 2010, 82(15): 155445
134. M. Ezawa, Phys. Rev. B, 2007, 76(24): 245415
135. J. Fernández-Rossier and J. J. Palacios, Phys. Rev. Lett., 2007, 99(17): 177204
136. W. L. Wang, S. Meng, and E. Kaxiras, Nano Lett., 2008, 8(1): 241
137. J. Jung and A. H. MacDonald, Phys. Rev. B, 2009, 79(23): 235433
138. T. Yamamoto, T. Noguchi, and K. Watanabe, Phys. Rev. B, 2006, 74: 121409(R)
139. Z. Z. Zhang, K. Chang, and F. M. Peeters, Phys. Rev. B, 2008, 77(23): 235411
140. X. Yan, X. Cui, B. S. Li, and L. S. Li, Nano Lett., 2010, 10(5): 1869
141. M. L. Sadowski, G. Martinez, M. Potemski, C. Berger, and W. A. de Heer, Phys. Rev. Lett., 2006, 97(26): 266405
142. M. Orlita, C. Faugeras, P. Plochocka, P. Neugebauer, G. Martinez, D. K. Maude, A. L. Barra, M. Sprinkle, C. Berger, W. A. de Heer, and M. Potemski, Phys. Rev. Lett., 2008, 101(26): 267601
143. C. Stampfer, S. Fringes, J. Güttinger, F. Molitor, C. Volk, B. Terrés, J. Dauber, S. Engels, S. Schnez, and A. Jacobsen, Front. Phys., 2011, 6(3): 271
144. K. Nakada, M. Fujita, G. Dresselhaus, and M. S. Dresselhaus, Phys. Rev. B, 1996, 54(24): 17954
145. K. Wakabayashi, M. Fujita, H. Ajiki, and M. Sigrist, Phys. Rev. B, 1999, 59(12): 8271
146. B. Wunsch, T. Stauber, F. Sols, and F. Guinea, Phys. Rev. Lett., 2008, 101(3): 036803
147. L. Yang, M. L. Cohen, and S. G. Louie, Phys. Rev. Lett., 2008, 101(18): 186401
148. T. Ohta, A. Bostwick, T. Seyller, K. Horn, and E. Rotenberg, Science, 2006, 313(5789): 951
149. E. V. Castro, K. S. Novoselov, S. V. Morozov, N. M. R. Peres, J. M. dos Santos, J. Nilsson, F. Guinea, A. K. Geim, and A. H. Neto, Phys. Rev. Lett., 2007, 99(21): 216802
150. J. B. Oostinga, H. B. Heersche, X. Liu, A. F. Morpurgo, and L. M. K. Vandersypen, Nat. Mater., 2008, 7(2): 151
151. K. F. Mak, C. H. Lui, J. Shan, and T. F. Heinz, Phys. Rev. Lett., 2009, 102(25): 256405
152. Y. Zhang, T. T. Tang, C. Girit, Z. Hao, M. C. Martin, A. Zettl, M. F. Crommie, Y. R. Shen, and F. Wang, Nature, 2009, 459(7248): 820
153. R. T. Weitz, M. T. Allen, B. E. Feldman, J. Martin, and A. Yacoby, Science, 2010, 330(6005): 812
154. E. V. Castro, K. S. Novoselov, S. V. Morozov, N. M. R. Peres, J. M. B. Lopes dos Santos, J. Nilsson, F. Guinea, A. K. Geim, and A. H. Castro Neto, J. Phys.: Condens. Matter, 2010, 22(17): 175503
155. L. M. Zhang, Z. Li, D. N. Basov, M. M. Fogler, Z. Hao, and M. C. Martin, Phys. Rev. B, 2008, 78(23): 235408
156. T. Wassmann, A. P. Seitsonen, A. M. Saitta, M. Lazzeri, and F. Mauri, Phys. Rev. Lett., 2008, 101(9): 096402
157. O. Voznyy, A. D. Güçlü P. Potasz, and P. Hawrylak, Phys. Rev. B, 2011, 83(16): 165417
158. K. A. Ritter and J. W. Lyding, Nat. Mater., 2009, 8(3): 235
159. D. K. Armani, T. J. Kippenberg, S. M. Spillane, and K. J. Vahala, Nature, 2003, 421(6926): 925
160. E. H. Lieb, Phys. Rev. Lett., 1989, 62(10): 1201